From THE DEPARTMENT OF CLINICAL NEUROSCIENCE
Karolinska Institutet, Stockholm, Sweden

METHODOLOGICAL ADVANCEMENTS IN DATA ANALYSIS AND QUANTITATIVE PERFORMANCE OF POSITRON EMISSION TOMOGRAPHY

Martin Schain

Stockholm, 2013

Cover Illustration:

The illustration on the cover page is a 3D-rendered PET image of the radioligand [^{11}C]flumazenil overlaid on an MRI. The image shows the distribution of $GABA_A$ receptors in the human brain. The image was processed by Carola Grahn.

Published by Karolinska Institutet. Printed by Larserics Digital Print AB

ISBN 978-91-7549-373-2

To my family.

”*The whole problem with the world is that fools and fanatics are always so certain of themselves, but wiser people so full of doubts.*”

-Bertrand Russel, 1872-1970

ABSTRACT

Positron emission tomography (PET) is a medical imaging modality with which neurophysiological functions can be studied. After a radio-labeled molecule is injected intravenously, it is transported by the blood stream to the target of interest. The radioactive atom of the molecule decays, resulting in two gamma rays that the PET system detects. Based on this measurement, an image can be reconstructed displaying the distribution of the radioligand, which in turn provides useful information regarding the underlying physiology.

This thesis focuses on methodological advancements in the quantification of PET data obtained from neurological studies. The work included in the thesis can be categorized into three sections. Section 1 comprises two studies (Study I and II) and focuses on the effect of the resolution of the PET system when quantifying the data. When using PET to study brain functions in for instance the brainstem, the structures of interest are small and therefore presumably affected by resolution. The results of study I showed that, using conventional methods for PET data analysis, the difference obtained between two PET systems with different resolution can be compensated for by applying algorithms that artificially compensate for resolution-induced image artifacts. This is an interesting finding as it enables data acquired in two different PET systems to be pooled into the same analysis, without introducing significant bias. In study II, we found that using a high resolution PET system, in combination with a noise suppression technique and a semiautomatic procedure to define regions of interests (ROIs), it is possible to accurately quantify radioligand binding in very small brain structures. The procedure allows for detailed mapping of the distribution of serotonin transporter in the brainstem, and may thus be used to help elucidate the role of the serotonin system in central nervous system disorders.

Section 2 targets the definition of ROIs required for analysis of PET data. Conventionally, ROIs are defined manually by a neuranatomically trained expert on MR images acquired from the same subject. This procedure is time consuming and introduces a large amount of user interaction in the data analysis, making it prone to rater bias. In study III, it is shown that manual ROIs can reliably be replaced with automated versions provided by the software package FreeSurfer or the Automated Anatomical Labeling (AAL) template. These automated methods provide objective and reproducible analysis of PET data.

In section 3, a new method to cluster the voxels of PET images is presented. This Pair-Wise Correlation (PWC) approach groups correlating voxels, either within or across subjects. The method is used for two different purposes. First, in study IV, the PWC method isolates the signal corresponding to arterial blood in the images. This image-derived blood signal provides the possibility to quantify PET data without measuring the radioactivity level in arterial blood, which significantly reduces the invasiveness during a PET examination. Second, in study V, the PWC method identifies a disease-specific pattern of amyloid-β plaque in patients with Alzheimer's disease. The pattern can in turn separate a group of AD patients from control subjects, suggesting that the PWC method may aid for early and objective detection of brain amyloid.

In conclusion, this thesis focused on validation and implementation of advanced tools for quantification of PET data. The results indicate that the methods included in this thesis provide improved quantification of PET data and can be used in clinical PET studies.

SAMMANFATTNING

Utvecklingen av medicinsk avbildning har under de senaste decennierna gjort anmärkningsvärda framsteg. Idag kan man studera såväl strukturer som funktioner av kroppens inre organ med mycket hög upplösning och känslighet. Olika avbildningsmetoder erbjuder olika sorters information, och kan ofta samverka till synergistiska effekter. För att studera strukturella förändringar i kroppen, till exempel vid benbrott eller hjärnblödning, kan magnetresonanstomografi (MR) eller datortomografi användas. Dessa avbildningstekniker tillhandahåller dock ingen information om kroppens funktion, d.v.s cellulära mekanismer såsom energikonsumption, syresättning och kommunikation mellan nervceller.

Positronemissionstomografi (PET) är en funktionell eller molekylär avbildningsmetod. PET bygger på att spårmolekyler administreras i kroppen, varpå den strålning som molekylerna ger upphov till registreras av PET-kameran. På så sätt kan distributionen av spårmolekylen i kroppen mätas, och med kunskap om spårmolekylens biologiska egenskaper kan slutsatser om kroppens funktioner dras.

Denna avhandling syftar till att förbättra de metoder som används för att kvantifiera PET-mätningar. Avhandlingen är indelad i tre delar. Del ett fokuserar till stor del på de begränsningar som PET-kamerans relativt dåliga upplösning sätter på kvantifieringen av PET data. I del ett visas bl.a. att förbättringar i upplösning från $\sim$4 mm till $\sim$2 mm minskar mätfelet, och att man med hjälp av algoritmer som artificiellt höjer bildupplösningen kan kompensera för den skillnaden. Den senare upptäckten möjliggör därmed att PET-data insamlad med olika system kan kombineras i samma studie, vilket underlättar exempelvis forskning bedriven vid flera forskningscentrum. Vidare så visas i del ett att PET-kameror med väldigt hög upplösning, tillsammans med metoder som förtrycker mätbrus kan användas för att kvantifiera koncentrationer av radioliganden i mycket små strukturer i hjärnan, vilket möjliggör detaljerad kartläggning av bl.a. hjärnstammens fysiologi.

I del två i avhandlingen så utvärderas två metoder för automatisk avgränsning av de hjärnregioner som ska inkluderas i analysen. Traditionellt sett så görs dessa avgränsningar manuellt, genom att regionerna ritas på MR-bilder. Ett sådant förfarande är dock begränsat av en rad faktorer. Bland annat medför det en stor del användarinteraktion, vilket kan introducera systematiska fel. Dessutom är det tidskrävande och försvårar därmed analys av stora mängder data. I del två påvisas att automatiska avgränsningsmetoder kan ersätta manuella, och därmed kan ovan nämnda begränsningar undvikas.

I del tre så beskrivs en helt ny metod för att representera PET-data. Metoden bygger på att alla parvisa korrelationer mellan PET-bildens bildpunkter beräknas, och sparas i en stor matris. På så sätt kan alla punkter som korrelerar med varandra identifieras, och specifika nätverk i hjärnan kan kartläggas. Metoden användes först för att identifiera bildpunkter som innehåller blod, för att på så sätt kringå behovet av att sätta artärnål under PET-mätningar. Sedan applicerades metoden på en grupp patienter med Alzheimer's sjukdom (AD) för att kartlägga hur de patologiska utfällningarna av s.k. amyloida plack var distribuerade i hjärnan. De kluster av amyloid som identifierades kunde sedermera användas för att på ett objektivt sätt och med goda marginaler separera en annan grupp patienter med AD från friska kontroller. Den föreslagna proceduren har således potential att underlätta ställandet av tidiga diagnoser, samt indikera huruvida individer befinner sig i riskzonen för att utveckla AD.

Sammanfattningsvis så innehåller avhandlingen utveckling och utvärdering av en rad metodologiska verktyg för analys av PET-data. Resultaten visar att dessa metoder medför förbättrad metodologi, och att de med fördel kan användas i kliniska studier.

LIST OF THESIS PUBLICATIONS

The following five papers are included after the summary chapter and are referred to by their roman numerals in the text.

I. **Martin Schain**, Miklós Tóth, Zsolt Cselényi, Per Stenkrona, Christer Halldin, Lars Farde, and Andrea Varrone. Quantification of Serotonin Transporter Availability With [^{11}C]MADAM – a Comparison Between the ECAT HRRT and HR Systems. *NeuroImage* **60**, 800-807 (2012).

II. **Martin Schain**, Miklós Tóth, Zsolt Cselényi, Ryosuke Arakawa, Christer Halldin, Lars Farde, and Andrea Varrone. Improved Mapping and Quantification of Serotonin Transporter Availability in the Human Brainstem with the HRRT. *European Journal of Nuclear Medicine and Molecular Imaging* **40(2)**, 228-237 (2013).

III. **Martin Schain**, Katarina Varnäs, Zsolt Cselényi, Christer Halldin, Lars Farde, and Andrea Varrone . Evaluation of Two Automated Methods for PET Region of Interest Analysis. *Submitted*

IV. **Martin Schain**, Simon Benjaminsson, Katarina Varnäs, Anton Forsberg, Christer Halldin, Anders Lansner, Lars Farde, and Andrea Varrone. Arterial Input Function Derived From Pairwise Correlations Between PET-image Voxels. *Journal of Cerebral Blood Flow and Metabolism* **33(7)**, 1058-1065 (2013).

V. **Martin Schain**, Anton Forsberg, Anders Lansner, Christer Halldin, Andrea Varrone, and Lars Farde. Amyloid Clustering for Classification of Alzheimer's Disease Based On Pairwise Correlations Between PET-image Voxels . *Submitted*

LIST OF NON-THESIS PUBLICATIONS

I. Balazs Gulyás, Adám Vas, Miklós Tóth, Akihiro Takano, Andrea Varrone, Zsolt Cselényi, **Martin Schain**, Patrik Mattson, and Christer Halldin. Age and disease related changes in the translocator protein (TSPO) system in the human brain: positron emission tomography measurements with [^{11}C]vinpocetine. *NeuroImage*. **356(3)**, 1111-21 (2011).

II. Balazs Gulyás, Miklós Tóth, **Martin Schain**, Anu Airaksinen, Adám Vas, Konstantinos Kostulas, Per Lindström, Jan Hillert, and Christer Halldin. Evolution of microglial activation in ischaemic core and peri-infarct regions after stroke: a PET study with the TSPO molecular imaging biomarker [^{11}C]vinpocetine. *J Neurol Sci.* **320(1-2)**, 110-7 (2013).

III. Magdalena Nord, Sjoerd J Finnema, **Martin Schain**, Christer Halldin, and Lars Farde. Test-retest reliability of [^{11}C]AZ10419369 binding to the $5\mathrm{HT}_{1\mathrm{B}}$ receptors in human brain. *Eur J Nucl Med Mol Imaging*, In press.

TABLE OF CONTENTS

LIST OF ABBREVIATIONS

1TCM	1 Tissue Compartment Model
2TCM	2 Tissue Compartment Model
5-HT	Serotonin
5-HTT	Serotonin Transporter
AAL	Automatic Anatomical Labeling
AD	Alzheimer's Disease
$B_{\max}$	Receptor Density
BP	Binding Potential
CNS	Central Nervous System
CSF	Cerebrospinal Fluid
CT	Computed Tomography
FBP	Filtered Back Projection
FWHM	Full Width at Half Maximum
GM	Gray Matter
GTM	Geometric Transfer Matrix
HRRT	High Resolution Research Tomograph
ICA	Independent Component Analysis
IDIF	Image-Derived Input Function
IRF	Impulse Response Function
K_D	Dissociation constant at equilibrium
LOR	Line Of Response
LSO	Lutetium Oxyorthosilicate
LYSO	Lutetium-yttrium Oxyorthosilicate
MCI	Mild Cognitive Impairment
MNI	Montreal Neurological Institute
MRI	Magnetic Resonance Imaging
OSEM	Ordered Subset Expectation Maximization
PD	Parkinson's Disease
PET	Positron Emission Tomography
PSF	Point Spread Function
PVE	Partial Volume Effect
PWC	Pair-wise correlation
ROI	Region Of Interest
SPECT	Single Photon Emission Computed Tomography
SPM	Statistical Parametric Mapping
SRTM	Simplified Reference Tissue Model
TAC	Time Activity Curve
V_T	Total Distribution Volume
WAPI	Wavelet-aided Parametric Imaging
WM	White Matter

1 INTRODUCTION

1.1 Rationale for this thesis

The evolution of medical imaging techniques has had a major impact on healthcare in the industrialized part of the world. The ability to visualize internal anatomy and physiology is frequently used today for both diagnostic and research purposes, at a steadily increasing rate. Until 2010, approximately 5 billion medical imaging investigations had been conducted worldwide, of which two thirds employed ionizing radiation [1]. Each of these measurements is associated with a cost, both from the biological impact of radiation on the human body, and economically. Methods used for analyzing the images must therefore be of the highest possible standard, in terms of providing reliable results and maximizing the amount of information extracted from each image.

Methodological development in medical science is however a never-ending task. The exponential improvement of processor power acquired over the last 60 years [2], together with advancements in related scientific disciplines such as physics and signal processing, enables a continuous refinement of imaging methodology. For positron emission tomography (PET), such advancements include improved detectors [3, 4] and system electronics [5], enhanced reconstruction strategies [6] to reduce the measurement noise and maintaining high resolution, as well as improved statistical tools for group analysis such as data mining [7] and clustering approaches [8]. Such analysis tools have during recent years gained remarkable attention in scientific communities. Today, hospitals and universities possess large archives of medical data, and these biobanks are predicted to be the core resources of medical research in the 21th century [9]. Possible applications of such resources are scientific group analysis with such statistical power that novel insights of biology can be gained, and systems that support clinical decisions [10] and treatment planning [11].

Both of these examples require that data acquired in various settings and locations can be directly compared. Measurements acquired on different systems, and analysis procedures relying to a large extent on manual user interaction, may prevent an unbiased pooling or comparison of data. It is therefore of important that measurement errors induced by the system are well understood and corrected, and that objective analysis approaches are available.

The general aim of this thesis was to develop and evaluate methodological tools for standardized and user-independent quantification of data acquired with PET. In study I, we investigated the difference in serotonin transporter density estimated from PET images acquired on PET systems with different resolutions, and showed that algorithms compensating for resolution-induced image artifacts could reduce that difference. This observation suggests that images from the two systems can be pooled into the same analysis, and thereby simplifies multi-center studies. In study II we developed a method that permits the quantification of serotonin transporter availability in the brainstem in a standardized way. In study III, we evaluated automated methods for objective definition of region of interests (ROIs). Automated definition of ROIs greatly reduces the time required for performing PET data analysis and reduces the need for user interaction in the analysis. In study IV, we developed a method for non-invasive measurement of the radioactivity concentration in the blood that can simplify the quantification procedure of PET data. Finally, in study V, we demonstrated how statistical approaches can be used to identify disease specific patterns in PET images acquired from a group of patients with Alzheimer's disease.

1.2 Applications of PET for neuroscience research

Unlike structural imaging modalities such as magnetic resonance imaging or computed tomography, PET is a functional imaging modality that measures brain function. More specifically, PET enables estimation of physiological parameters, such as density of neurotransmitter receptors or transporters, blood flow, glucose metabolism, oxygen utilization, and neuroinflammation. The ability to study such functional processes in the brain in vivo has provided new knowledge in several fields of clinical neuroscience, including neurodegenerative diseases such as Alzheimer's disease [12], psychiatric disorders such as major depression [13], and cognitive neuroscience [14, 15]. Moreover, the possibility to measure changes in various neurotransmitter systems in vivo has made PET a valuable tool for psychiatric drug research, as the technique enables accurate quantification of drug delivery and occupancy of the target of interest [16].

1.3 PET methodology

1.3.1 Radioactive nuclides

The acquisition of PET data relies upon the decay of certain unstable isotopes such as ^{11}C, ^{18}F, ^{13}N, and ^{15}O. When these isotopes decay, a positron is created and emitted. A radioligand – a molecule in which one of the atoms is replaced by a radioactive isotope – is used as imaging marker. The properties of the molecule determines the target site to which the radioligand will bind. For instance, raclopride is a synthetic compound, which binds to the dopamine D_2 receptor, that can be combined with ^{11}C (denoted [^{11}C]raclopride) to measure the dopamine D_2 receptor availability in vivo. Examples of other radioligands include [^{11}C]MADAM which binds to the serotonin transporter, [^{11}C]flumazenil which binds to the $GABA_A$ receptor, and [^{11}C]PiB which binds to amyloid β-plaques, expressed in the brains of patients with Alzheimer's disease (AD).

1.3.2 PET data acquisition

A PET radioligand is normally administered intravenously and delivered via the blood stream to the target organ, such as the brain. As the radioactive atom attached to the radioligand decays, it releases a positron that travels a short distance (approximately 1 mm, depending on the isotope, see section 1.3.4) before interacting with an electron. Upon interaction, the particle pair annihilates, and a photon pair is created (Figure 1). The energy conserved in the masses of the electron-positron pair (1.02 MeV) defines the wavelength of the photons, which are emitted in a random direction and separated by approximately $180^{\circ} \pm 0.25^{\circ}$ [17]. The uncertainty of the exact angle is called the non-collinearity effect, and its extent depends upon the isotope used (see further section 1.3.4).

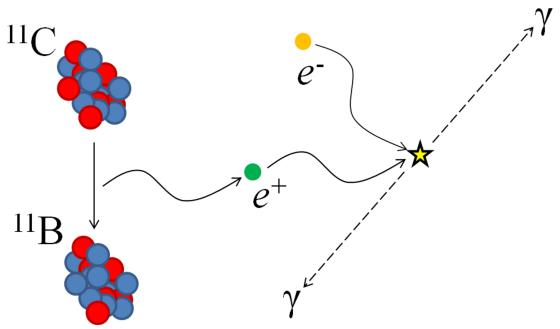

Figure 1. An unstable nucleus decays, producing a positron which in turn interacts with an electron. The annihilation of the two particles produces a photon pair.

The two photons propagate through tissue, skull, and air, and are eventually detected by an opposing pair of detectors in the PET system. The *Line Of Response* (LOR) is defined as the imaginary straight line connecting the detectors, and it is assumed that the radioactive decay occurred somewhere along that line. The simultaneous detection of the two photons is referred to as a coincident count, a somewhat unusual interpretation of the word *coincidence*. During a PET measurement, a substantial amount of LORs are recorded by the PET system, forming the basis upon which the PET image can be reconstructed (see section 1.3.3)

1.3.3 PET data reconstruction

The PET system records photon pairs created by the annihilation of the positron-electron pairs. Thus, information obtained from the acquisition consists of projections from the three dimensional object positioned in the system upon the array of detectors surrounding that object. The word *tomography* is derived from the Greek word *tomos*, meaning a slice or a disk, and *graphein*, meaning to write. Accordingly, PET image reconstruction algorithms recreate the object giving rise to the measured projections by reconstructing a set of 2D images (slices) which, when stacked on top of each other, compose the reconstructed 3D image. The projection p of a slice onto the detector is composed by the line integral for all parallel LORs for each angle θ, as illustrated in figure 2. The position of each LOR in the

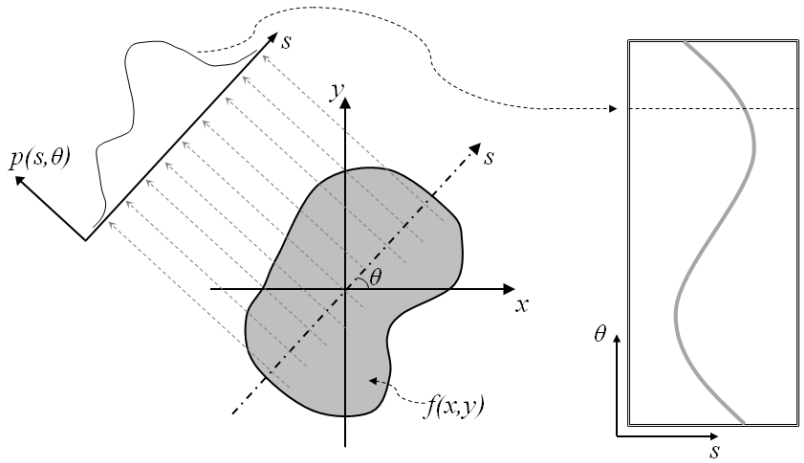

Figure 2. The 1D projection p of the 2D object $f(x, y)$ for a certain angle θ. The projections of all angles are stored in the sinogram, illustrated to the right.

bundle of rays is given by s. Using this nomenclature, the transform of $f(x, y) \rightarrow p(s, \theta)$ can be obtained using the *Radon transform*,

$$p(s,\theta) = \int_{-\infty}^{\infty}\int_{-\infty}^{\infty} f(x,y)\delta(x\cos(\theta) + y\sin(\theta) - s)dxdy. \quad (1)$$

Based upon the projection p, different strategies can be employed in order to recreate $f(x, y)$. This thesis will only discuss the filtered back projection approach (FBP) and the ordered subset expectation maximization (OSEM) approach, as all data included in the thesis are reconstructed using one of these two methods.

Filtered backprojection The filtered backprojection (FBP) is an analytical solution which maps the projections back onto the image domain to recreate the object, $p(s,\theta) \rightarrow f(x,y)$. The *central slice theorem* states that the 1D fourier transform of a projection at a certain angle is equivalent to a line profile through the 2D fourier transform of the object through the same angle. Therefore, by fourier transforming all projections, letting the transformed projections fill the 2D fourier space at all angles, and finally applying the inverse 2D fourier transform, the original object is reconstructed. Since fourier space is filled radially, the information will not be evenly distributed. Information at the center of the fourier space will be oversampled, and more sparse closer to the edges. In order to compensate for this inhomogeneous distribution of data, each projection is filtered prior to being positioned in the 2D fourier space. In theory, a normal ramp filter solves the oversampling issue by suppressing the central fourier space and amplifying the edges. Mathematically, the filtered projection $p_f(s,\theta)$ is given by

$$p_f(s,\theta) = \mathscr{F}^{-1}(|h| \cdot \mathscr{F}(p(s,\theta))), \tag{2}$$

where $\mathscr{F}$ denotes the fourier transform, $|h|$ is the 1D ramp filter, and $p(s,\theta)$ is defined in equation 1. Once the filtered projections are calculated, the 2D object $f(x,y)$ is obtained from the filtered backprojection formula,

$$f(x,y) = \int_0^{\pi} p_f(s,\theta) d\theta. \tag{3}$$

One caveat of the FBP reconstruction approach is that since the ramp filter amplifies the signal in the edges of the fourier space, it amplifies the high frequent noise. This makes the reconstruction problem ill-posed, and regularizations have been introduced to stabilize the algorithm with regards to noisy data. For instance, the Hann window function can be used as an apodizing function that acts as a low-pass filter to suppress the amplified noise component.

Ordered Subset Expectation Maximization The OSEM algorithm is an iterative reconstruction method based upon the maximum likelihood expectation maximization (ML-EM) method of statistics. It requires that the system matrix $\mathbf{H}$ is known, where element $H_{i,j}$ contains the probability of a photon emitted from voxel j to be detected in projection i. The reconstruction problem thus takes the form $P = \mathbf{H}X$, where P is the measured projections and X is the image to be reconstructed, represented as a single column matrix. The number of photons emitted from voxel j towards projection i is modeled as a Poisson-distributed stochastic variable, which enables a formulation describing the probability relation between the measured projections and the true activity in j. Maximizing the expectation value of the probability function results in the following update rule for the estimated activity in voxel j,

$$x_j^{new} = \frac{x_j^{current}}{\sum_i H_{i,j}} \sum_i \left\{ H_{i,j} \frac{p_i}{\sum_k H_{i,k} x_k^{current}} \right\}, \tag{4}$$

where p_i is the measurement made in the i:th projection. Conceptually, equation 4 describes that the current estimates of the voxel values are forward-projected to sinogram space ($\sum_k H_{i,k} x_k^{current}$). Secondly, the ratio between measured projections and the forward-projected estimates in the voxels are calculated, $\left(\frac{p_i}{\sum_k H_{i,k} x_k^{current}} \right)$. This ratio illustrates

how well the estimated image corresponds with the measured projections. Thirdly, the ratio is backprojected into image space, $\left(\sum_i H_{i,j} \frac{p_i}{\sum_k H_{i,k} x_k^{current}}\right)$, and finally multiplied by the current estimate in voxel j, resulting in equation 4 [18].

One drawback of the traditional ML-EM reconstruction is that it requires many iterations before convergence is obtained, resulting in a long reconstruction time. OSEM solves this issue by categorizing the projections into subsets, and then utilizing only one subset at a time in equation 4. For instance, the initial image estimate is normally just an array of constant values, which together with the projections stored in subset 1, is used to create a first image estimate. This estimate is in turn used as input in equation 4, together with the projections stored in subset 2. The updated image will be used again as an input, together with the projections stored in subset 3, and so on, until all N subsets have been used, which defines one iteration. The subsets of projections are interlaced. For example, if there exist a total of 9 projections and 3 subsets, subset 1 will include projection 1, 4 and 7; subset two will include projection 2, 5, and 8; and subset 3 will hold projections 3, 6, and 9. For the HRRT at Karolinska Institutet, 10 iterations in combination with 16 subsets provide an optimal trade-off between high recovery of radioactivity and short reconstruction times [19].

1.3.4 Resolution of PET images

Despite the major improvements achieved in PET image acquisition and reconstruction during the last decade, the resolution of PET images are still significantly lower than in structural imaging modalities such as CT and MRI. Radioactive decay is a Poisson-distributed stochastic process, and hence, a certain degree of noise already exists at the level of the decay of the nuclei. Furthermore, the PET system measures the LOR through which the annihilation of the positron-electron pair occurred. However, the positron created during a decay event has a certain level of kinetic energy and will travel a short distance before it annihilates. Thus there will be a discrepancy between position of the annihilation and the position of the decay, where the latter is of primary interest. The distance between two events depends on the energy of the positron, which varies for different radionuclides. For the nuclides commonly used in PET, i.e. ^{11}C and ^{18}F, the average energy is in the order of a few hundred keV, giving rise to distances of up to 1 mm [20–23].

The positron-electron pair will experience a momentum prior to annihilation. The principle of conservation of momentum leads to an uncertainty in the exact angle separating the two emerging photons, which is called the non-collinearity effect [24]. The extent to which the non-collinearity effect impacts PET images cannot easily be assessed. In 1965, Colombino *et al.* approximated that the angular deviation from 180° follows a Gaussian distribution with 0.47° FWHM [25]. This number is often referenced to, despite that the measurement was conducted in pure water and that the chemical properties of the human body might influence the angular distribution. In more biologically relevant conditions, the angular deviation from 180° may in fact be approximately 10% higher than in water [26]. In addition to the deviation from 180°, the actual measurement error due to the non-collinearity of the photons depends on the diameter of the detector ring.

Apart from the positron travel and non-collinearity effect, the measurement of coincident photon pairs are also affected by random and scattered events, as shown in figure 3. During a PET examination, the fraction of scattered events can be up to 50% of the total counts [27]. It is however impossible to determine whether an event is scattered or not,

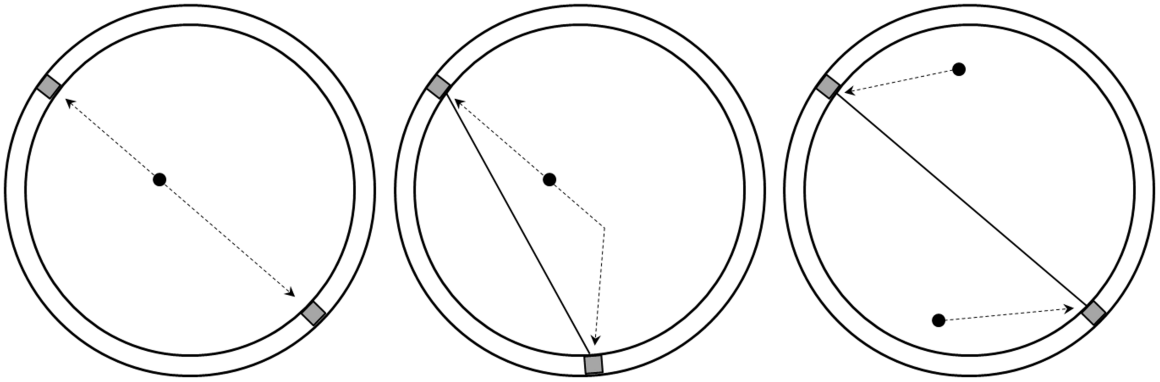

Figure 3. The ideal coincidence is shown in the left panel. The other panels illustrate the erroneous LOR resulting from a scattered event (middle panel), and a random coincidence (right panel).

as long as the energies of the photons are within the energy window of the system. The correction for scatter is therefore performed by removing the estimated scattered fraction from the projection. Different strategies have been suggested for estimating fraction of scattered events. An accurate but computationally expensive alternative has proven to be Monte Carlo simulation of the scattered photons [28]. Other suggested approaches are the Gaussian fit method [29] and the single scatter simulation method [30]. For the HRRT at KI, the scatter distribution is assumed to be Gauss-shaped, and the contribution is estimated by modifying the function parameters. The parameters are found iteratively by comparing the measured radioactivity in a region close to the edge and a region in the center of a uniformly filled cylindrical phantom. The iteration stops when similar radioactivity values are obtained in both regions.

The right panel of figure 3 illustrates a LOR generated after a *random* coincidence, i.e., a LOR generated after detection of two photons not originating from the same decay. To minimize the rate of random events (R), a short time window is used during which two detected photons are considered coincident. Moreover, R can be estimated directly by recording rates of single events (i.e., detection of only one photon).

As a $\gamma-$ ray propagates through tissue and skull, its intensity I is attenuated according to the *Beer-Lambert* law,

$$I(x) = I_0 e^{-\int_0^x \mu(x)dx}. \tag{5}$$

If the attenuation coefficient μ is known for every point in the image, the attenuation of the rays can be compensated for. Normally a transmission scan precedes the emission acquisition in order to retrieve the so-called μ-map. The transmission is performed either with a single source (as in the case of the HRRT) or with rotating rod sources (as in the case in the ECAT HR system). Either way, the decay of the sources produces γ rays with energies similar to those produced after an annihilation, so that they are within the system's energy window. The μ-map can then be reconstructed in order to retrieve the scaling factors needed to compensate for the signal attenuation in the PET image.

Clearly, the final resolution of a PET image is affected by several parameters. In addition to the physical entities discussed above, electronic noise from the circuits, detector dead time, and intrinsic radioactivity in some scintillators also impact the PET image resolution. It has been suggested that, for a given detector size d, detector array diameter D, positron travel distance r, and additional factors (such as gaps between the detecor blocks),

the resolution Γ of a PET system can be predicted by

$$\Gamma = \xi \sqrt{\left(\frac{d}{2}\right)^2 + (0.0022D)^2 + r^2 + b^2}, \tag{6}$$

where the value of ξ is determined by the reconstruction, and empirically found to be ≈ 1.25 [31]. This is interpreted as, if an infinitesimal point source was positioned in the system, the resulting PET image would be blurred to the extent that if a line profile was drawn through the blurred point source, it would display a FWHM of Γ mm. The spreading of the point source is called a *point spread function* (PSF). The FWHM of the PSF is conventionally used as a measure of PET system resolution, and is typically in the order of a few mm.

1.3.5 Region of interest analysis

In many PET applications, accurate quantification requires information regarding the kinetic properties of a radioligand. The measurement is therefore conducted over time interval; normally 60-90 minutes post radioligand delivery, during which both the uptake and washout of the compound can be studied. Dynamic PET data are therefore 4D images, where the fourth dimension typically consists of 20-40 time steps (called time frames). Regional *time activity curves* (TACs) are obtained by placing a *region of interest* (ROI) over a set of image elements (voxels), and calculating the average voxel value for those voxels, at each time step. The regional TAC will then contain information regarding the temporal behavior of the radioligand in the specific region. Due to the poor spatial resolution of PET, images from other modalities, such as MRI or CT, are normally used to define the ROIs. The ROIs are normally delineated manually on the MR images and then applied to the PET images. Manual ROI delineation is however associated with several problems, which are discussed further in section 1.4.4.

1.3.6 Kinetic modeling

The overall objective of quantitative analysis of PET data is to determine a mathematical model that describes the measured regional TACs and that differentiates the radioligand concentration in various tissue pools (or compartments). Depending on the properties of the radioligand, a different number of compartments is required (see figure 4 for the most commonly used models). For all models, the radioligand concentration in arterial plasma, C_p, serves as a driving force, or the model's input.

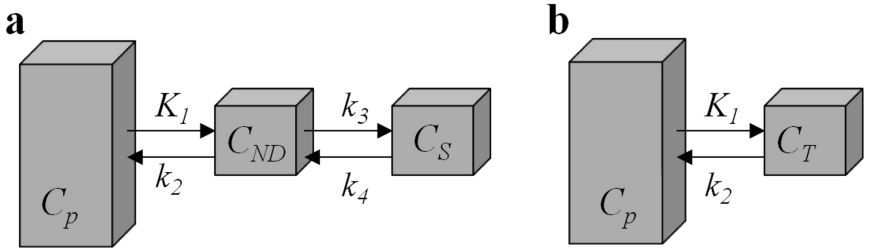

Figure 4. Common kinetic models used for quantitative analysis of PET data. **a**: 2-tissue compartment model, where C_{ND} denotes concentration of non-displaceable radioligand (i.e., free and non-specifically bound), and C_S denotes concentration of specifically bound radioligand. For radioligands with rapid transfer between C_{ND} and C_S, the model can be simplified to the 1-tissue compartment model, shown in **b**.

Regardless of which method is used, the concentration measured in an ROI contains contribution from all tissue pools and from the radioligand in the vascular tissue within the ROI. Based on the assumptions introduced by the models and on the Fick principle, a set of differential equations can be formulated describing the transfer of the radioligand between the compartments. The solution to these equations provides an analytical expression describing the concentration of radioligand that is specifically bound to the target site over time,

$$C_S(t) = C_p(t) \otimes \sum_{n=1}^{N} a_n e^{-b_n t}. \tag{7}$$

The number of exponentials with which the input function $C_p(t)$ is convolved depends on which model is used, typically one exponential per compartment [32]. In equation 7, the term $\sum_{n=1}^{N} a_n e^{-b_n t}$ is said to be the *impulse response function* (IRF). For the special case of 1TCM, the IRF is $K_1 e^{-k_2 t}$, with the rate constants defined by figure 4. For the other models, the coefficients a_n and b_n corresponds to combinations of rate constants. Exact values for a_n and b_n can be estimated by fitting equation 7 to the measured TAC.

A common measure of interest is the *total distribution volume*, V_T. The distribution volume is defined as the amount of plasma required to account for the amount of radioligand in 1 cm^3 of brain tissue [33]. Mathematically, V_T is defined as ratio at equilibrium between total tracer concentration in tissue to that in plasma, and can be calculated as a combination of the rate constants. V_T may also be determined using graphical analysis approaches, such as the *Logan plot* [34], which can be derived directly from the differential equations obtained from the 1TCM or the 2TCM. After applying the fundamental theorem of calculus and rearranging, the following expression is obtained

$$\frac{\int_0^t C_T(\tau)d\tau}{C_T(t)} = V_T \frac{\int_0^t C_p(\tau)d\tau}{C_T(t)} - \frac{1}{k_2}. \tag{8}$$

The plot $\frac{\int_0^t C_T(\tau)d\tau}{C_T(t)}$ versus $\frac{\int_0^t C_p(\tau)d\tau}{C_T(t)}$ will become linear after a certain time, normally denoted t^*. The slope of the linear curve equals V_T [32]. Since this procedure requires measurement of C_p, it is sometimes referred to as the invasive Logan plot. Fitting a linear curve is far less computationally demanding than iterative fitting techniques required to fit equation 7, which renders graphical analysis approaches suitable for the generation of parametric images (see further section 1.3.7).

Another important parameter for neuroreceptor studies is the ratio $\frac{k_3}{k_4}$ from the 2TCM in figure 4, which is related to the *binding potential* (BP). BP provides an important theoretical connection between imaging and in vitro receptor binding, via $BP = \frac{B}{F} = \frac{B_{\max}}{K_D}$, where B denotes the concentration of bound receptors, F the concentration of free radioligand, $B_{\max}$ the total receptor density, and $\frac{1}{K_D}$ the binding affinity of the radioligand [35]. In vitro, both B and F can be measured, while in PET imaging, the concentration of free radioligand is not available. Instead, a common parameter of interest is the BP_{ND}, defined as

$$BP_{\mathrm{ND}} = \frac{C_S}{C_{ND}} = f_{\mathrm{ND}} \frac{C_S}{C_F} = f_{\mathrm{ND}} \frac{B_{\max}}{K_D} \tag{9}$$

where f_{ND} denotes the fraction of the non-displaceable compartment corresponding to free radioligand ($C_F = f_{\mathrm{ND}} C_{\mathrm{ND}}$, see figure 4a).

It is possible to calculate BP_{ND} directly from the kinetic rate constants in figure 4. The differential equation for the specifically bound compartment in the 2TCM is

$$\frac{dC_S(t)}{dt} = k_3 C_{ND}(t) - k_4 C_S(t), \tag{10}$$

which, at equilibrium, results in $\frac{C_S}{C_{\mathrm{ND}}} = \frac{k_3}{k_4}$. Since equation 9 states that $BP_{\mathrm{ND}} = \frac{C_S}{C_{ND}}$,

$$BP_{\mathrm{ND}} = \frac{k_3}{k_4}. \tag{11}$$

Regardless of whether the goal is to estimate the individual rate constants or only the V_T, the radioactivity concentration in arterial plasma, $C_p(t)$ needs to be known. However, if there is a region in the brain which is devoid of the target neuroreceptor, that region can serve as a reference in which C_{ND} can be measured and thereby enable estimation of BP_{ND} without any knowledge of C_p. The most common reference region models are shown in figure 5.

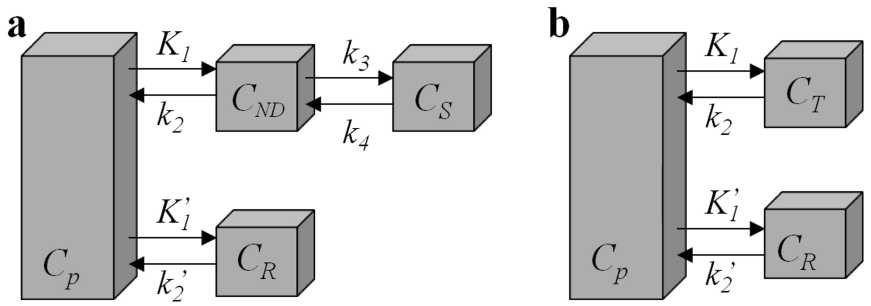

Figure 5. Kinetic models using concentration in reference tissue, C_R, as an indirect input function. **a**: 4 parameter reference tissue model. **b**: Simplified reference tissue model.

Based on the 4 parameter reference tissue model [36] shown in figure 5a, it is possible to derive a relationship between C_T and C_R, including the 6 rate constants. However, the two rate constants K_1 and K_1' only appear as a ratio. Therefore Lammertsma and colleagues defined $R_1 = \frac{K_1}{K_1'}$ and assumed that the volume of distribution of the *non-specifically bound* tracer is the same in the target and in the reference region,

$$\frac{K_1}{k_2} = \frac{K_1'}{k_2'} \longrightarrow k_2' = \frac{k_2 K_1'}{K_1} = \frac{k_2}{R_1}. \tag{12}$$

This modification reduced the number of fitting parameters to 4: R_1, k_2, k_3, and BP_{ND} $(= \frac{k_3}{k_4})$.

The four parameter reference tissue model is stable in the estimates of BP_{ND}, but the reliability of the other parameters is limited [37]. For radioligands that can be properly described by the 1TCM, and for which a proper reference region exists, the 4 parameter reference tissue model can be simplified even further, into the simplified reference tissue model (SRTM), shown in figure 5b. The equation describing the radioligand concentration becomes

$$C_T(t) = R_1 C_R(t) + \left\{ k_2 - \frac{R_1 k_2}{1 + BP_{\mathrm{ND}}} \right\} C_R(t) \otimes e^{-\frac{k_2 t}{1+BP_{\mathrm{ND}}}}, \tag{13}$$

where the three unknown parameters R_1, k_2, and BP_{ND} are estimated via fitting.

Lastly, the Logan plot can also be modified so that it utilizes a reference region instead of the measured radioactivity in plasma [38]. By applying equation 8 to the reference region C_R, an analytical expression for C_p as a function of C_R can be obtained. Inserting that expression back into equation 8 results in following the expression

$$\frac{\int_0^t C_T(\tau)d\tau}{C_T(t)} = DVR\frac{\int_0^t C_R(\tau)d\tau}{C_T(t)} + \text{intercept}. \tag{14}$$

Similarly to the invasive Logan plot, the slope of the linear part of the plot $\frac{\int_0^t C_T(\tau)d\tau}{C_T(t)}$ versus $\frac{\int_0^t C_R(\tau)d\tau}{C_T(t)}$ holds the parameter of interest, in this case the *distribution volume ratio*, $DVR = \frac{V_T}{V_{\text{ND}}} = BP_{\text{ND}} + 1$. Logan plot using a reference region rather than blood samples is referred to as the non-invasive Logan plot.

1.3.7 Parametric mapping

Conventional methods of analyzing PET data perform the quantification on the ROI level, i.e., the parameter of interest, such as V_T or BP_{ND}, is calculated for each ROI. Consequently, all information about heterogeneity of radioligand binding within the ROI is lost. Attractive alternatives are parametric mapping approaches. These algorithms calculate a value for the outcome measure in each voxel and thereby creates 3D maps of parameter distribution (see figure 6).

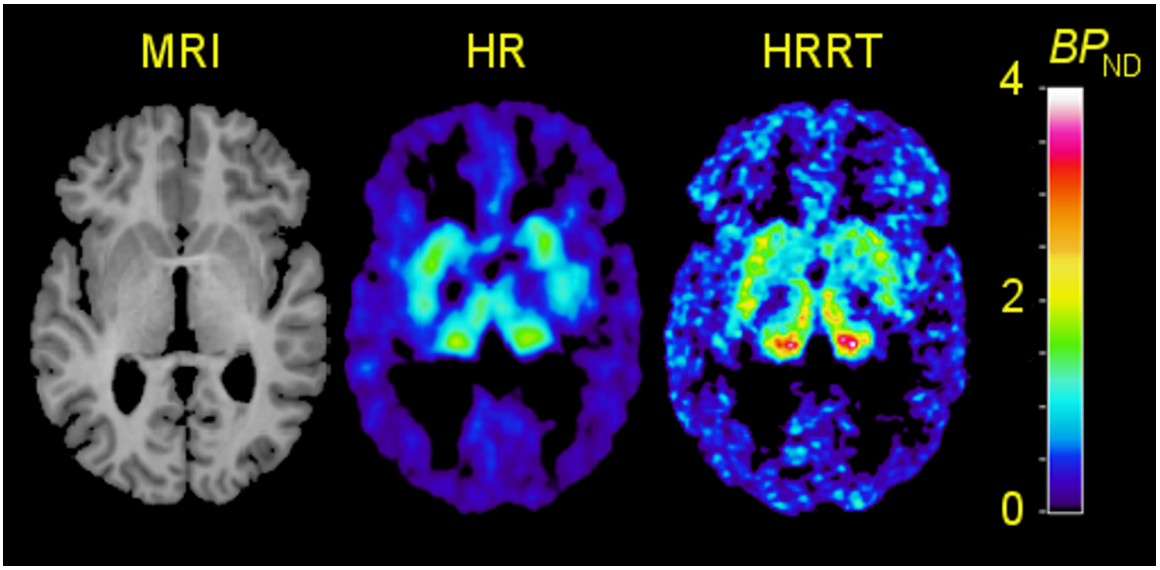

Figure 6. Parametric images showing the distribution of binding potential of [^{11}C]MADAM (binding to the serotonin transporter) acquired with the HR and the HRRT system.

Estimating outcome measures at the voxel level is associated with a high computational cost. Therefore, due to the non-linear fitting procedures, compartmental modeling has not proven to be a viable strategy for generation of parametric maps. Moreover, since the TAC of each voxel is associated with a high noise level, the algorithm needs to apply noise reduction filters in order to derive meaningful estimates. Examples of algorithms which successfully fullfill these criteria is the Gunn's basis function method [39] and the wavelet-aided parametric imaging approach (WAPI) [40].

The latter of the two is used in study II and study V of this thesis. WAPI utilizes the important feature of the wavelet transform, that spatial information of the signal is kept after the transformation, whereas it is lost in the traditional fourier transform. More specifically, the coefficients of a wavelet transform contain information about the frequencies of the signal at a certain location (called "spatial frequencies"). This feature enables the wavelet transform to separate the different components of the signal based on their frequency. The noise component of the signal is represented by high frequencies, whereas the real (noise-free) signal, consists of lower frequencies. Consequently, the noise component of the signal can be identified and discarded.

The transformation into wavelet coefficients is realized in an iterative process separating the high from the low spatial frequencies using wavelet filters with finite support. The high frequency component is retained, while the low frequency component is separated at the next iteration into high and low frequencies. The most suitable length of the wavelet filter (*filter kernel length*, fkl), as well as the optimal number of iterations (*decomposition depth*, dd) may depend upon the PET image resolution and the reconstruction procedure, and should thus be optimized for each PET system (see further section 3.7).

WAPI uses the Logan Graphical Analysis approach (equations 8 and 14). Since the wavelet transform is a linear operation that is applied on each frame separately, the temporal dynamics of the tracer are unchanged in the transformation. This enables the linear fitting of equation 8 and 14 to be performed on the wavelet coefficients rather than on radioactivity values of the voxels. The coefficients displaying low values are discarded from the fits, and the remaining slopes are converted back into image space. The resulting image will thus display the distribution of V_T or DVR, depending on whether the invasive (equation 8) or non-invasive (equation 14) method was used.

1.4 PET methodology advancements

1.4.1 High resolution research tomograph (HRRT)

The High Resolution Research Tomograph (HRRT), a state-of-the-art system for human brain PET imaging, was installed at Karolinska Institutet in 2007 and was operational from 2008. The transition from the fourth generation PET systems, such as the ECAT EXACT HR to the HRRT, introduced an improvement in resolution, from ~ 4 mm FWHM in the HR to ~ 2 mm in the HRRT. This improvement was a result of several new features in both hardware and software.

First, the gantry size of the HRRT is substantially smaller than that of the previous generation system (35 cm vs 56 cm in gantry diameter [41, 42]). The smaller gantry size reduces measurement errors caused by the non-collinearity effect and photon scattering (see section 1.3.4). Second, the HRRT contains substantially more and smaller crystals than its predecessor. The detectors of the HRRT are organized in an octagonal array of detector heads. Each head consists of 9×13 detector blocks, each with an 8×8 array of detectors. Third, each detector consists of 2 layers of scintillating crystals: Lutetium oxyorthosilicate (LSO) in the innermost layer, and lutetium-yttrium oxyorthosilicate (LYSO) in the outermost layer. The double layer geometry enables the measurement of depth of the photon interaction within the crystal and thereby reduces the parallax effect [43]. The HRRT uses 119808 detectors in total, each with a volume of $2.15 \times 2.15 \times 10$ mm^3 and with a 2.4 mm center-to-center distance between crystals.

Fourth, the HRRT acquires data in list mode, meaning that each coincident and single count is recorded in a long list. This representation of the recorded data provides more flexibility when reconstructing the images, as the definition of time frames can be determined post acquisition. The standard procedure for reconstructing HRRT data at Karolinska Institutet is 3D-OP-OSEM, including modeling of the system PSF. The implemented PSF model is described in detail by Comtat et. al. [44], and differs from the original implementation described by Sureau et al. [45] with regards to the projectors used (see section 1.3.3). In the model, the PSF is approximated by a superposition of two isotropic 3D Gaussian functions, with FWHM1 of 2.1 mm and FWHM2 of 5.9 mm, and Gauss1 to Gauss2 ratio of 0.01 [19]. With regards to the number of iterations needed before convergence of the OSEM, Varrone et al. showed that only marginal improvement in resolution was achieved when the number of iterations was increased above 10, whereas the noise level significantly increased [19]. Therefore, the standard number of iterations was set to 10. Taken together, the final resolution of the HRRT at the Karolinska Institutet was found to be 1.5 mm FWHM in the center of the field of view, and 2.4 mm at 10 cm distance from the center.

1.4.2 Partial volume effect correction

The term partial volume effect (PVE) for medical imaging originally referred to the signal artifacts originating from the relatively large voxel sizes of the images. The volumes of the voxels of early generation PET and MR systems were so large that they could contain a significant proportion of two or more tissue types. The volume constituting the voxel was therefore said to consist of two or more partial volumes, which affected the reliability of the values of individual voxels, particularly for voxels close to tissue boundaries. With the development of higher resolution imaging systems, the voxel sizes has decreased, and modern system are associated with voxel volumes of ~ 1 mm^3. Consequently, the original definition of PVE is today not a major issue.

For emission tomography modalities however, there exists also another type of signal artifact, which is also called PVE. The limited resolution of these modalities causes the radioactivity to spill over between structures. The effect becomes particularly pronounced for brain structures which are associated with a high density of binding sites, and are surrounded by low density structures. Depending on the resolution of the system, the extent of radioactivity spilled out may cause the measured radioligand binding in such structures to be significantly underestimated.

Figure 7 illustrates how in the (1D) PET image, the signal measured from each of the structures is contaminated by the signal from the neighboring structures. Moreover, the maximal radioactivity estimated in each structure is reduced, which is particularly pronounced in the high density region ($x_3 \leq x \leq x_4$). In a PET image, all neighboring regions are thus contaminated by each other. By assuming that the resolution of the system is known, and that the boundaries between contaminating structures can be defined, this aspect of PVE can be corrected. In this thesis, three different methods for PVE corrections are used. Two are so called voxel-based methods, meaning that they produce a new, PVE corrected image. The third method is ROI-based, and thus affects the TACs rather than the actual PET image. All methods assume that for each measured PET image I^{PET}, there exists a true image I^{true}, which, when convolved with the system PSF (here denoted h to

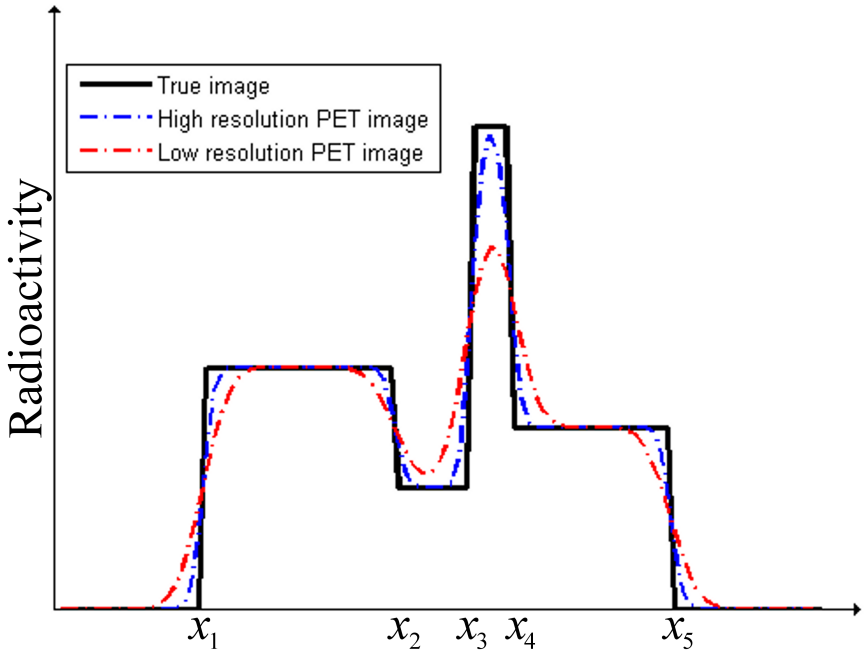

Figure 7. Illustration of the partial volume effect for PET images. The signal obtained from neighboring structures with different density of receptors is contaminated. The higher the resolution of the system, the less the extent of PVE. If the resolution of the system and the spatial location of the regions (the coordinate x_i in this figure) is known, the images can be corrected for PVE.

be consistent with previous publications), are equal

$$I^{PET} = I^{true} \otimes h. \tag{15}$$

Thus, correcting for PVE is a deconvolution problem.

Meltzer's method The method proposed by Meltzer et al. [46] assumes homogeneous binding in brain tissue and no binding in cerebrospinal fluid (CSF). The only border which needs to be PVE-corrected is that between brain tissue and the CSF present in the ventricles and outside the brain. To define that border, segmented and coregistered MR images can be used. To estimate the amount of signal loss, an image mask is created, such that it contains 1s in voxels corresponding to brain tissue, and 0s everywhere else (I_{tissue}). This mask is subsequently artificially degraded to the resolution of the PET, by convolution with the system PSF ($I_{Mask} \otimes h$). Given the resolution of the system, the degraded mask holds information regarding how much signal has spilled out from each voxel. Thus, the PET image corrected with Meltzer's approach is retrieved via

$$I^{true} = \frac{I^{PET}}{I_{tissue} \otimes h}. \tag{16}$$

Müller-Gärtner's method Müller-Gärtner's approach (MG) [47] assumes that radioligand binding in gray matter (GM) is homogenous, binding in white matter (WM) is homogenous, and that binding in CSF is non-existent. The MG method is designed to improve quantification of radioligand binding only in GM, and thus aims at correcting the border between GM and WM, and between GM and CSF. The border between GM and CSF can

easily be corrected for in a manner similar to that used in Meltzer's approach. To correct the border between GM and WM, however, the MG approach assumes that the value in every WM voxel can be replaced by the average WM signal, which can be obtained from an uncontaminated part of the middle of the WM, typically the centrum semiovale.

If k_{WM} denotes the average signal in WM, and I_{GM} and I_{WM} denote masks for GM and WM, respectively, then the amount of contamination from WM in the signal measured from GM can be estimated by $k_{WM}\{I_{WM} \otimes h\}I_{GM}$. This quantity needs to be subtracted from the original PET image. Similar to Meltzer's approach, the degradation of the GM mask to the resolution of the PET provides information regarding the loss of signal in each GM voxel. The final equation describing the correction procedure for the MG approach becomes

$$I^{true} = \frac{I^{PET} - k_{WM}\{I_{WM} \otimes h\}I_{GM}}{I_{GM} \otimes h}. \tag{17}$$

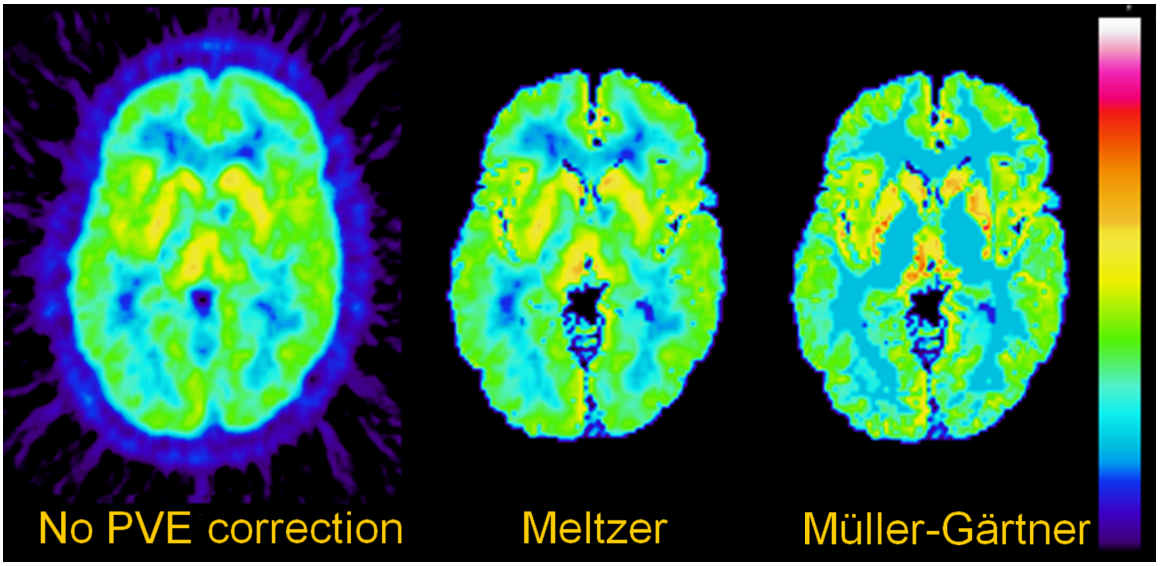

Figure 8. Summation PET image of [^{11}C]MADAM acquired with the HR system, before and after correction for Partial Volume Effects.

Rousset's method The method described Rousset et al. [48] differs from the previous methods in that it does not create a PVE-corrected PET image. Instead it operates only on the values measured in each of the ROIs. The method assumes that the radioactivity value measured in ROI i (x_i), is a weighted combination of the true value in ROI i (y_i), and the true value in all other ROIs. The weights a_{ij} determine the impact of ROI j on the measurement of ROI i. More specifically,

$$\begin{aligned} x_1 &= a_{11}y_1 + a_{12}y_2 + \cdots + a_{1n}y_n \\ &\vdots \\ x_n &= a_{n1}y_1 + a_{n2}y_2 + \cdots + a_{nn}y_n \end{aligned} \tag{18}$$

or in matrix form

$$\underbrace{\begin{bmatrix} x_1 \\ \vdots \\ x_n \end{bmatrix}}_{\mathbf{x}} = \underbrace{\begin{bmatrix} a_{11} & \cdots & a_{1n} \\ \vdots & \ddots & \vdots \\ a_{n1} & \cdots & a_{nn} \end{bmatrix}}_{\mathbf{A}} \times \underbrace{\begin{bmatrix} y_1 \\ \vdots \\ y_n \end{bmatrix}}_{\mathbf{y}}. \tag{19}$$

The weights, i.e., the elements of $\mathbf{A}$, are determined by calculating the amount of cross contamination between each of the ROI pairs. An estimate of the cross contamination can be obtained by smoothing a mask of the ROI i with the PSF, and calculating the amount that the ROI contaminates all other ROIs [49].

Once all the elements of $\mathbf{A}$ are known, the true radioactivity values are obtained by

$$\mathbf{y} = \mathbf{A}^{-1}\mathbf{x}. \tag{20}$$

In some publications, this method is referred to as the *geometric transfer matrix* (GTM) method, where the geometric transfer matrix is the matrix $\mathbf{A}$ above [50, 51].

Drawbacks The main drawback of the above-mentioned methods is that assumptions need to be formulated a priori regarding the borders along which PVE occurs. For the Meltzer and the Müller-Gärtner methods, these borders are defined from segmented MRI and are therefore dependent on accurate coregistration of the MRI. In addition, the Meltzer approach only corrects spill-over of radioactivity between brain tissue and CSF, and therefore, the effect of applying the method may not be very well pronounced, particularly for sub-cortical regions. The MG approach has some limitations in terms of reliability because it may sometimes overcorrect the data [52]. This overcorrection is often visible in the PVE-corrected images; in thin cortical regions embedded between CSF and WM, individual voxels can gain over 100% of the measured value in the PVE correction step, making the data less reliable (see figure 8). For the method described by Rousset, the main limitation is that each voxel in the PET image must be assigned to exactly one ROI to be correct. Voxels which are not assigned to an ROI may contaminate other ROIs, but the contamination will not be corrected for when applying equation 20. This limitation introduces the need for using ROI templates to make the method practically feasible.

Other methods There have been suggested methods that remove the limitations described above. The convolution problem described in equation 15 can be addressed using deconvolution techniques. For instance, Teo et al [53] and Tohka and Reilac [54] applied the Van Citter deconvolution algorithm. The Van Citter deconvolution is an iterative scheme, with the goal of estimating the true PET image I^{true} so that the blurred image $I^{true} \otimes h$ matches the measured image I^{PET}. The basic idea is to minimize the function $(I^{PET} - I^{true} \otimes h)^2$, by finding the I^{true} for which the derivative of the function becomes 0. Apart from the original publication by Tohka and Reilhac, only a few publications use the the Van Citter deconvolution scheme [55]; overall, the algorithm has not been frequently utilized.

Another sophisticated approach was proposed by Bouisson et al., which, by wavelet transforming high resolution images such as MR or CT images, transfers the high frequency information (such as edges and details) into the PET images [56, 57]. A potential drawback of such a procedure is that it will introduce image artifacts when there are slight errors in

the co-registration. The method has also been criticized for not being based on a solid theoretical foundation [58].

1.4.3 Imaging the serotonin transporters in the brainstem

The serotonin neurotransmission system is widely distributed in the brain. It is involved in numerous physiological functions, including mood and social interaction [59], cognition [60], thermoregulation [61], sleep [62], and pain [63]. Serotonin originate from the raphe nuclei in the brainstem, from where it is projected to essentially all cortical regions. The raphe nuclei are of moderate-size, and distributed along the midline of the brainstem in the rostro-caudal extension. The rostral structures (i.e., the caudal linear, the dorsal raphe, and the median raphe nucleus) project primarily to the forebrain, whereas the more caudal complex (raphe magnus, raphe obscurus, and raphe pallidus) project to the brainstem itself and to the spinal cord [64, 65]. Abnormal serotonergic transmission from the raphe nuclei has been implicated in several psychiatric and neurological conditions, including Alzheimer's disease [66], Parkinson's disease [67], depression [68], and suicidal tendencies [69]. In addition, loss of serotonergic neurons in the median and the caudal raphe nuclei has been observed in patients with Parkinson's disease [70]. Thus detailed mapping of serotonergic transmission in the raphe is necessary for several areas of neuroscience.

Accurate in vivo imaging of the raphe nuclei using PET has the potential to elucidate the role of the serotonin system in neurological disorders. However, the limited spatial resolution of PET has traditionally prevented accurate quantification of radioligand binding in small brain structures, such as the raphe nuclei. As described in section 1.4.2, the small volume of the raphe in combination with a low resolution system lead to significant spill-out of radioactivity, making changes in receptor or transporter densities difficult to detect. Moreover, since the raphe nuclei are not easily visible on MR images, they cannot be accurately delineated. Consequently, the PVE-correction techniques discussed in 1.4.2 cannot be applied. The only possible solution for accurate measurement of receptor or transporter availability in the raphe is a high system resolution.

In theory, the resolution of the HRRT is high enough to resolve the nuclei of the raphe. However, Leroy et al. reported that the voxel-to-voxel noise level of the HRRT is too high for reliable quantification of small brainstem regions using conventional ROI-based kinetic modeling [71]. In that paper, the authors concluded that parametric imaging, and noise suppression techniques are necessary for reliable quantification in small brainstem regions.

The serotonin transporter (5-HTT) has frequently been used as a marker for serotonergic neurotransmission. The radioligand [^{11}C]MADAM [72] binds selectively to the 5-HTT and is therefore suitable for measuring 5-HTT in the raphe. In addition, the wavelet aided parametric imaging approach (WAPI) for generation of parametric images [40] successfully reduces the noise level in PET data, while maintaining reasonable resolution [73]. Hence high resolution PET imaging using HRRT together with WAPI may be suitable for quantification of radioligand binding in small structures of the brainstem. In study II, this procedure is undertaken, in combination with an in-house developed semi-automatic procedure for delineation of small ROIs, in order to examine the possibility of quantifying 5-HTT density in the raphe nuclei.

1.4.4 Automatization of ROI delineation

The number of applications of PET in neuroscience research has steadily increased over the last decade. The unique capability of PET to study functional processes in the living human brain has provided useful insights into many fields of neuroscience including psychiatric and neurodegenerative disorders, as well as cognitive neuroscience [12, 14, 74]. The increased use of PET in neuroscience research has lead to the acquisition and accumulation of a substantial amount of PET data, acquired by different researchers and for different scientific purposes. Nevertheless, if analyzed in a stream-lined fashion, the PET data currently available can be combined into datasets from which novel research questions can be addressed.

As described in section 1.3.5, the definition of regions of interests (ROI) is a required step in conventional PET data analysis. Traditionally, ROIs are manually delineated, meaning that a neuroanatomically trained expert draws the ROIs by hand upon MR images. This procedure introduces a large amount of user interaction in the data analysis, making it prone to rater bias. The procedure may thus show low reproducibility. In addition, manual definition of ROIs is time consuming and prevents swift analysis of data. These limitations become particularly challenging when the dataset at hand is large and pooling of data from a large number of subjects is necessary. In order to generate databases of PET data accumulated over the years, we must bypass the manual ROI delineation step in the analysis workflow.

Automatic methods to define the ROIs would overcome these limitations. During the last decade, several software packages have been developed, which are based upon MRI templates and provide a set of automatically generated ROIs. Although such software would be of general benefit for PET research, applications of automated methods for ROI delineation are still limited in the literature. One possible explanation is that since the definition of ROIs is a crucial step in the analysis, automated methods need to be thoroughly evaluated before they can be applied routinely.

In study III of this thesis, two such automated methods for ROI delineation are evaluated. The methods are the Automatic Anatomic Labeling (AAL) template [75] and the FreeSurfer package [76]. The AAL is based on an existing template of pre-defined ROIs. The template is stored in the general MNI space [77], and when applied to a subject, the template is warped to the space of the individual MRI. AAL is easily accessible in the Statistical Parametric Mapping (SPM) toolbox for MATLAB. The FreeSurfer package is a more sophisticated software package, that was originally developed for cortical reconstruction, volumetric analysis, and segmentation of structural MR images. The whole FreeSurfer package is freely available online (http://surfer.nmr.mgh.harvard.edu/), and the technical details can be found in the following references [78–97].

Both AAL and FreeSurfer are associated with benefits and potential drawbacks. AAL is fast and easy to use, and thereby provides means to quickly derive TACs from a large number of subjects. A potential limitation is, however, that the normalization of the template might not be accurate for individuals whose brain structures deviate substantially from the template, for instance patients with severe atrophy or other structural changes. In contrast, the FreeSurfer registration, which is based upon the individual cortical folding patterns rather than image intensities, may provide increased stability for subjects with severe atrophy. However, FreeSurfer is associated with a substantially higher computational load than the AAL, requiring up to 20 hours of processing time per subject [98, 99].

The aim of study III was therefore to validate and compare the performance of the two automated methods for routine analysis of PET data.

1.4.5 Image-derived input functions

As described in section 1.3.6, in absence of a suitable reference region, the radioligand concentration in arterial plasma needs to be known for full quantification of PET data. The concentration of the unchanged radioligand in arterial plasma is used as the *input function* for the kinetic models described in section 1.3.6. This arterial input function is normally acquired by measuring the radioactivity level in blood samples obtained from an arterial catheter. This procedure is associated with several limitations. Arterial cannulation is a laborious procedure for the research personnel, and often found uncomfortable, or even painful, for the patients. Moreover, to capture the kinetics of the initial bolus of radioactivity, the arterial sampling needs to be performed at such high frequency that special blood sampling equipment is required. Arterial sampling is also sensitive to errors and introduces an increased risk for adverse events. A non-invasive procedure to estimate the input function would be preferable.

A suggested solution has been to estimate the input function directly from the PET image, and two different categories of approaches have been proposed. The first strategy is to combine (manual or automatic) delineation of ROIs for the arteries with tools that compensate for signal artifacts, and the second strategy is to "un-mix" the mixed signals of the PET image.

Methods for applying the first strategy have been developed by a large number of researchers for various radioligands [100–107]. The most straight-forward procedure in order to segment the carotid artery is to use a coregistered MRI from which the carotid artery can be easily segmented [101, 104]. From the MR image, information regarding the length and width of the carotid can be accurately determined, which can be used to compensate for signal loss. However, most coregistration techniques don't provide reliable alignment of the vessels, because 1) most of the existing coregistration algorithms assume that the MR and PET images can be aligned using rigid body transforms (which may be true for the brain itself but not for the neck region due to different positioning of the patient in MR and PET acquisitions), and 2) the calculations are performed using structures above the carotids. Fung et al. even found that the individual carotids needed to be coregistered separately in order for their MR-based method to work [104].

Another possibility is to define the ROI directly on the PET image itself, which has the benefit that no coregistration to MR images is needed. The obvious drawback is that the carotid artery is not easily detectable in a dynamic PET image. Chen et al. suggested to use a summation image of the early time frames, during which the injected bolus of activity was still in the vessels [108]. In this time window, the vessels are clearly visible, enabling manual delineation of the carotid artery ROI directly on the PET image. In the original publication by Chen et al., ROIs covering the vicinity of the artery were also manually delineated in order to estimate and correct for signal contamination.

The procedure to only use the early time frames for obtaining the carotid artery ROI was later adopted by several researchers, which replaced the manual delineation step with automatic alternatives. First, Chen et al. applied independent component analysis (ICA) on the summation image in order to obtain the artery ROI [109]. Later, Mourik et al. proposed to define the ROI on the summation image of early frames, as the 4 hottest voxels

in each plane, ranging from the level of the Circle of Willis to approximately 10 cm down. [110]. Hahn et al. developed a sophisticated approach feeding the early frames into a linear discriminant analysis algorithm together with a set of tissue classes, including vascular tissue. The procedure enabled identification of the voxels resembling blood properties in the early part of the acquisition [107].

One problem of the above methods is that they only consider the radioactivity values in the beginning of the measurement. Thus, voxels which have high values in early frames are included in the ROI, regardless of the shape of the TAC during the remainder of the measurement. All voxels that experience noisy TACs in later time frames will be kept, which may introduce an unnecessary amount of noise in the blood TAC. This problem becomes particularly challenging for HRRT data, in which the voxel-to-voxel noise level is considerably high. In an ideal algorithm, the whole blood TAC should be considered, so that the final ROI only includes voxels displaying blood-like behavior during the whole measurement. One such application was developed by Liptrot et al. [111]. In that article, the authors applied K-means clustering [112] on a set of PET images of [^{18}F]altanserin. In K-means clustering, each cluster center (i.e., the "true" TAC) is defined as the mean of the cluster members (i.e., the TACs assigned to the cluster). The final solution is reached after iterating through a loop that reassigns the voxels and updates the centers. After the algorithm is stabilized, the cluster centers correspond to the final tissue TACs.

The second strategy to estimate the blood signal is to "un-mix" the assumed mixed signals in the PET image. More specifically, the TAC of each voxel can be considered to be a linear combination of a set of underlying "true" TACs. Thus, by applying unmixing algorithms, the true TACs, of which the blood TAC is one, can be identified. Approaches belonging to this category are for example those by Naganawa et al. [113], and Bodvarsson et al. [114]. Naganawa et al. used a set of [^{18}F]FDG images, on which ICA was applied to identify the underlying two independent components, which were assumed to be "tissue" and "blood". A similar approach was implemented by Bodvarsson et al. where the signal separation of the voxel TACs was performed with matrix factorization with non-negativity constraints. For both Naganawa's and Bodvarsson's approaches, the shape of the signal is maintained, whereas information regarding the amplitude is lost.

Although signal separation techniques seem like an attractive option, the number of publications utilizing similar methods is limited, possibly due to their level of complexity. Since the clustering is based on the kinetic properties of the tracer, it is likely that the algorithm needs to be tuned for each radioligand. Also, noise properties and system resolution are likely to affect the behavior of such an algorithm, and thus, differences in performance between different PET systems and reconstruction methods are expected.

Despite the efforts undertaken during the last decade, applied PET studies utilizing image-derived input functions (IDIFs) are rare. Due to the low resolution and high noise levels associated with PET, several methods have shown low reproducibility when implemented by other research groups [115], leading to a growing skepticism towards the feasibility of the concept. In a recent review article, Zanotti-Fregonara et al. stated that the difficulties associated with deriving an IDIF are too many and too difficult considering the potential benefit [116]. However, most attempts to derive blood curves have been performed on PET data acquired on systems with significantly lower resolution compared with the HRRT. The carotid artery is a small and elongated structure, with approximately 5 mm diameter [117], with complex hemodynamic patterns [118]. Thus system resolution is likely a fundamental factor for accurate measurement of the IDIF.

1.4.6 Amyloid imaging

Advancements in radioligand development have provided suitable imaging biomarkers for studying brain physiology and disorders affecting the central nervous system (CNS). Development of radioligands binding specifically to amyloid-β plaques represent one of the major advancements. Amyloid imaging using PET can quantify the distribution and density of amyloid plaques in the human brain. It has consequently proven to be a valuable tool for studying Alzheimer's disease (AD), which is characterized by the deposition of amyloid plaques. Over the years, several new radioligands binding specifically to amyloid-β plaques have been developed, for instance [^{18}F]AZD4694 ([^{18}F]NAV4694) and [^{11}C]AZD2184 [119, 120]. In addition to their specific binding to amyloid, these radioligands have both shown low binding values in healthy subjects [121, 122].

AD is the most common form of dementia, accounting for a substantial proportion of the total 35 million individuals estimated to suffer from dementia [123]. In 2010, the worldwide cost associated with dementia was estimated to $604 million [124] and is predicted to increase along with the prevalence of AD due to the increasing life expectancy. The cognitive decline associated with the disease involves suffering for the affected individuals, as well as for their close ones, and it motivates the large amount of research and resources devoted to developing effective treatment strategies and diagnostic tools. To date, none of the existing drugs have shown any long-term effect in the progression of the disease. One possible explanation is that the conducted trials selected moderately affected individuals, whose disease progression is difficult to revert [125]. The ability to identify individuals at risk of developing AD at an earlier time point is thus a prerequisite for testing treatment strategies [126] and may even facilitate early diagnosis of the disease.

Typically, the deposition of amyloid plaques appears years or even decades before any cognitive symptoms are detected [126–129]. Amyloid imaging using PET may therefore serve as an early biomarker by enabling in vivo quantification of amyloid-β deposition in brain. The first PET measurement of amyloid deposition was performed by Klunk et al. in 2004 [130] and amyloid imaging has since then been widely applied in both research and in clinical trials [131]. Recently, the FDA approved the clinical use of amyloid PET as an aid to exclude the possibility of AD among individuals with established dementia [132].

Unfortunately, high levels of amyloid have been shown not to be specific for AD. In addition to patients with a clinical diagnosis of AD, about 20-30% of healthy elderly individuals and about 50-60% of individuals with mild cognitive impairment (MCI) have been shown to have non-negligible levels of amyloid-β [133–137]. Several studies have also reported difficulties in separating controls subjects from AD patients with minor levels of amyloid-β in the early course of the disease [138–140]. Thus the problem is multifaceted. First, deposition of amyloid-β in the brain may be interpreted as a biomarker for AD, but it does not necessarily exclude the possibility of the subject being healthy. Second, how do we define a threshold for classifying subjects as amyloid positive or negative?

The second question has traditionally been addressed using ROI-based analysis, followed by application of empirically defined thresholds. This method of differentiating between amyloid positive and negative individuals has repeatedly been conducted with a varying degree of success, often resulting in overlaps between the groups [137–139, 141]. A potential explanation is that the formation of amyloid-β plaques does not follow the conventional boundaries defining the brain regions, making traditional ROI-based analysis suboptimal. Thus, new, objective ways are needed for identification of important brain re-

gions (or voxels) in which the differences between AD patients and controls are systematic and as evident as possible.

2 AIMS

The overall aim of this thesis was to validate established methods and to develop new methodological tools for quantification and analysis of PET data. More specifically, the aims were the following:

- To evaluate the effect of improved resolution on the measurement of 5-HTT availability.
- To evaluate and validate existing methods for correcting the partial volume effect.
- To develop a method enabling quantification of radioligand binding in small brain structures.
- To evaluate and validate existing methods for automated delineation of regions of interest for the analysis of PET data.
- To develop a method to obtain the image-derived arterial input function from dynamic PET data.
- To develop an objective method for classifying individuals as amyloid positive or negative.

3 MATERIALS AND METHODS

3.1 Rationale for selection of radioligands

Study I The purpose of study I was to compare the quantitative performance between the HR and the HRRT PET systems. Previous comparisons have been conducted focusing either on the cortical areas using the $GABA_A$ radioligand [^{11}C]flumazenil [142] or on sub-cortical areas using [^{11}C]PE2I, a radioligand that binds to the dopamine transporter [71]. These radioligands provide high target-to-background ratio, but they are either concentrated to the sub-cortical regions (striatum and midbrain for [^{11}C]PE2I) or more uniformly distributed throughout the brain [^{11}C]flumazenil). In study I, our interest was specifically to assess the effect that improved resolution had on the quantification of radioligand binding in brain regions with different size and different receptor densities. The radioligand [^{11}C]MADAM [72] was used as it provides signal from cortical *and* sub-cortical brain regions of different sizes and different serotonin transporter (5-HTT) densities.

Study II The purpose of study II was to develop a method for accurate quantification of serotonin transporter availability in the small nuclei in the brainstem. The radioligand [^{11}C]MADAM was selected, since it binds selectively to the 5-HTT [72].

Study III The purpose of study III was to validate FreeSurfer and the AAL template for automatic definition of ROIs in PET data analysis. Since the performance of the automated methods may vary across regions, the analysis would benefit from including a large number of ROIs. Therefore, data acquired using radioligands for two targets having different anatomical distribution were included in the study. First, the 5-HT_{1B} receptor radioligand [^{11}C]AZ10419369 [143] was selected due to the wide distribution of 5-HT_{1B} receptors across brain regions [144, 145]. In addition, the presence of 5-HT_{1B} receptors in vascular tissue [146] may "contaminate" the regional TACs and thereby influence the performance of the automated methods. Second, to evaluate whether brain atrophy affects the performance of the automated methods, AD patients and control subjects measured with the amyloid-β radioligand [^{11}C]AZD2184 [147] were included in the study.

Study IV The purpose of study IV was to validate the use of image-derived input functions as a substitute for arterial sampling. For this purpose, [^{11}C]flumazenil was chosen because its quantification often requires an input function; the suitability of pons as a reference region has been questioned [148]. In addition, [^{11}C]AZ10419369 was included in order to evaluate whether venous sampling can be used as a substitute to arterial sampling. This is possible since the metabolism of [^{11}C]AZ10419369 is negligible in humans. The total radioactivity in plasma can therefore approximate the input function without the need for metabolite correction.

Study V The purpose of study V was to identify the disease specific pattern of amyloid deposition among AD patients and to utilize that pattern in order to classify unknown subjects. To avoid a bias in the evaluation, two different datasets were required; one for determining the network (i.e., train the classifier) and one for testing it. To train the algorithm, PET images obtained using the amyloid-β radioligand [^{18}F]AZD4694 [120] were

used. For testing purposes, PET images acquired using the radioligand [^{11}C]AZD2184 [149] were used.

3.2 Research participants

This thesis to a large extent encompasses PET data acquired in different research projects. All procedures were approved by the Ethics Committee of the Stockholm Region, and the Radiation Safety Committee of the Karolinska University Hospital. All studies were performed in accordance with the ethical principles that have their origin in the Declaration of Helsinki and that are consistent with ICH/Good Clinical Practice. Written informed consent were obtained from all subjects prior to initiation of the studies For details regarding ages, injected radioactivities, specific radioactivities, and injected masses, please see the corresponding article/manuscript in the appendix.

Study I and II Study I and II includes 6 male control subjects that were healthy according to medical history, physical examination, ECG, and MRI. All subjects were examined twice on the same day, once using the HRRT and once using the HR system. For each subject, there was a 3.5 h interval between the measurements.

Study III Study III includes a total of 41 subjects, of which 20 were examined using the HRRT and remaining 21 were examined using the HR PET system. Of the 41 subjects, 15 were examined using [^{11}C]AZ10419369 and 26 were examined using [^{11}C]AZD2184. Of the subjects examined with [^{11}C]AZD2184, 9 subjects were healthy according to medical history, physical examination, blood and urine screening analyses, and MRI. The remaining 17 subjects were patients fulfilling the DSM-IV criteria for AD. The data used in study III were acquired in 5 separate studies [121, 122, 149–151].

Study IV Study IV includes a total of 12 subjects, all of which were examined using the HRRT. Of the 12 subjects, 6 were examined using [^{11}C]flumazenil, and 6 were examined using [^{11}C]AZ10419369. All subjects were healthy according to psychiatric and medical history, physical examination, laboratory testing, ECG, and MRI. The [^{11}C]flumazenil dataset consisted of baseline measurements in an occupancy study which is not yet published. The [^{11}C]AZ10419369 dataset was acquired in an academic study [151].

Study V Study V includes PET data from a total of 26 subjects, all examined using the HRRT. Sixteen subjects (10 AD patients and 6 controls) were examined using [^{18}F]AZD4694 and 16 subjects (11 AD patients and 5 controls) were examined using [^{11}C]AZD2184 (i.e., 4 AD patients and 2 controls were examined with both radioligands). The data in study V was acquired in two previously published studies [121, 122].

3.3 Data acquisition and reconstruction

All PET examinations included in this thesis were performed at the Karolinska Institutet PET center, located at the Karolinska University Hospital, Solna, Sweden. An individual plaster helmet was made for each subject to restrain the head and to prevent head motion during the PET scan [152]. In all cases, the tracers were intravenously administered as bolus injections after which the intravenous line was immediately flushed with saline.

This thesis encompasses PET data acquired in the ECAT EXACT HR system and the ECAT HRRT system (for scanner description of the HRRT, see section 1.4.1). All HR data were reconstructed using filtered back projection with a Hann filter of 2 mm cut-off frequency. All HRRT data were reconstructed using 3D ordinary poisson ordered subset expectation maximization, with PSF modeling, and 10 subsets and 16 iterations (see further section 1.3.3). For studies I, II, and IV, radioactivity levels in arterial blood were measured via an automatic blood sampling system (ABSS, Alogg Technology, Mariefred, Sweden) for the first five minutes, followed by manual arterial sampling at the midpoint of each time frame. Input functions were obtained by correcting the measured radioactivity level in arterial blood with the plasma fraction (i.e., plasma-to-blood ratio), and with the non-metabolized (parent) fraction.

Each study utilizes coregistered T_1-weighted MR images. For all studies, MR images were acquired on a 1.5 T GE signa system (GE medical systems, Milwaukee, WI, USA). In addition, for a few of the subjects included in study III and V, MR images were acquired using a 1.5 T Siemens Avanto system (Siemens Medical Systems, Erlangen, Germany), and one of the subjects included in study 4 was imaged using a 1.5 T Gyroscan Intera system (Philips Medical Systems, Best, The Netherlands). All MR images were coregistered to the PET image and segmented into gray matter, white matter, and cerebrospinal fluid, using Statistical Parametric Mapping 5 (SPM5, Wellcome Department of Cognitive Neurology, University College, London, UK).

3.4 Definition of regions of interest

Manual ROIs were used in studies I, III-IV, and were delineated using the in-house software Human Brain Atlas [153]. In study II, the included ROIs were delineated using a semi-automatic algorithm, which is explained in detail in section 3.7.2. In study III, both manually defined ROIs, and automated ROIs obtained with AAL and FreeSurfer were used (see further section 1.4.4). Study V included two manually defined ROIs which were manually delineated using Human Brain Atlas in order to generate the clusters (cerebellum as a reference region for WAPI, and posterior cingulate cortex as a seeding region to the PWC method). The clusters obtained from the PWC method were also used as ROIs for separation between AD patients and control subjects.

3.5 Partial volume effect correction

Correction for partial volume effects were applied in studies I and IV. In study I, the purpose was to compensate for the effect of disparate resolutions on the outcome measures obtained from the HR and the HRRT systems. Therefore, both HR and HRRT data were corrected using the PVE correction techniques described by Meltzer et al [46], and Müller-Gärtner et al. [47]. Both methods are described in detail in section 1.4.2.

In study IV, the signal obtained from the carotid artery ROIs was corrected for PVE using a modified version of the geometric transfer matrix (GTM) approach proposed by Rousset et al. [48]. The modification was introduced because the amount of spill-out of radioactivity from the carotid ROI varies throughout the PET measurement. In the initial phase when the radioactivity is still in the vessels, the spill-out is a major issue. At later time points, the radioactivity gradient between the vessels and their vicinity is smaller and could potentially be neglected. Therefore, only the first 3 minutes of the acquisition were

corrected for partial volume effects using the GTM method reduced to one compartment (i.e., only correcting for spill-out from the ROI), and a $2 \times 2 \times 2$ mm FWHM Gaussian filter. The width of the filter was set slightly higher than the measured system resolution, since the carotid artery is not in the center of the field of view.

3.6 Kinetic and graphical analysis

Several different outcome measures and models are used in this thesis. Each of the used models are explained in section 1.3.6. In study I and III, regional BP_{ND} is calculated using the SRTM. In study IV, regional V_T is calculated using the Logan Graphical Analysis approach. In studies II and V, the quantification is based upon parametric images of BP_{ND}, which are calculated using the non-invasive Logan Graphical Analysis approach and the cerebellum as a reference region (see section 1.3.7). Lastly, for the [^{11}C]AZD2184 data included in study III, regional DVR is estimated by dividing the area under the curve (AUC) of the target TAC to that of the reference region TAC over a specific time interval (in this case, 15-45 minutes post injection). This method has previously been described as a suitable approach for quantification of [^{11}C]AZD2184 data [149].

3.7 Parametric imaging

Studies II and V were quantified using parametric images obtained with WAPI. As described in section 1.3.7 and 1.4.3, the performance of WAPI depends upon the length of the wavelet filter (*filter kernel length*, *fkl*) as well as upon the number of iterations (*decomposition depth*, dd). Cselényi et al. have previously concluded that for HR data, an *fkl* of 22 together with a dd of 2 provided the highest possible recovery of regional BP_{ND} [40]. However, the optimal parameter settings for WAPI depend upon the system resolution, as well as the noise properties in the images, and thus need to be optimized for each system. In order to identify the most suitable parameter combination for HRRT images, the procedure described below in section 3.7.1 was undertaken.

3.7.1 Optimization of wavelet-aided parametric imaging for HRRT

In a systematic approach to identify *fkl* and dd for the HRRT data, parametric images were generated for numerous parameter combinations, when $14 \leq$ *fkl* ≤ 40 and $2 \leq dd \leq 6$. Regional BP_{ND} was estimated from each image using one large ROI, consisting of the frontal and temporal cortex, and in one small ROI, consisting of the dorsal brainstem. Both ROIs were manually delineated on the MR image. For the same regions, regional BP_{ND} was also estimated using conventional ROI-based graphical analysis with non-invasive Logan plot, and the percent difference in BP_{ND} estimated with the two methods was calculated. The combination of parameters that provided the best overall agreement with the ROI-based graphical analysis was selected for further analysis.

3.7.2 Delineation of small brain structures

As described in section 1.4.3, accurate quantification 5-HTT density in the raphe nuclei is of great importance for the study of the serotonin system in physiological and pathological conditions, but PET imaging of such small structures has traditionally been obstructed by the limited resolution of PET. Although the resolution of the HRRT is high enough

to properly resolve the different nuclei of the raphe, it has previously been shown that conventional analysis of regional TACs is not suitable for small ROIs due to the high voxel-to-voxel noise level of the HRRT [71]. A suitable alternative is to use parametric imaging in combination with noise suppression techniques.

To estimate the BP_{ND} of [^{11}C]MADAM in the raphe, an ROI delineation procedure for accurate definition of very small ROIs was developed. The procedure requires a parametric image and a coregistered MRI, and is as follows:

1. Using both the parametric image and the coregistered MRI, the top and bottom slice of the structure of interest is identified.

2. On each of those two slices, a rectangle is drawn covering the structure.

3. A bounding box is defined as the volume between the two rectangles, and is retrieved via linear interpolation over all intermediate planes.

4. The bounding box is eroded, so that all voxels with a BP_{ND} value lower than a predefined threshold are excluded from the ROI. The threshold is defined so that the volume of the final ROI coincides with the known volume of the structure.

5. Finally, the eroded ROI is applied to the parametric PET image.

The ROI delineation procedure is shown in figure 9. Since the method is based upon applying a threshold, one obvious drawback is that the method requires a rather high signal from the structure to be delineated. ROIs for structures associated with a low signal are at risk of being scattered (non-continuous) and thereby, might not reflect radioligand binding in a clearly defined area.

3.8 The pairwise correlation (PWC) approach

The pairwise correlation (PWC) method is used for two different purposes in study IV and study V. In Study IV, the PWC method is used to identify all voxels displaying blood-like behavior in order to estimate the image-derived input function. In study V the same method is used in order to localize the disease specific pattern of amyloid deposition, which characterizes Alzheimer's disease. The PWC method is an adoption of an algorithm originally developed by Benjaminsson et al. for the analysis of resting-state fMRI data [154]. Several modifications were introduced in order for the algorithm to be applicable to PET images. Initially, the algorithm by Dr Benjaminsson calculated the mutual information between each voxel pair in the image. Mutual information however requires quantization of voxel values, which is not an appropriate strategy for PET imaging. Several different measures were evaluated, and the Pearson correlation coefficient was determined to be the most suitable statistical measure. In addition, the original algorithm includes a second step, where multidimensional scaling was applied in order to detect patterns in the data. Although that method provided very good results for fMRI images, it has not yet been shown to work well for PET.

3.8.1 The general PWC method

The PWC method is characterized by the calculation of the correlation matrix $\mathbf{M}$, such that element i, j of $\mathbf{M}$ contains the Pearson Correlation Coefficient between the TACs x_i and

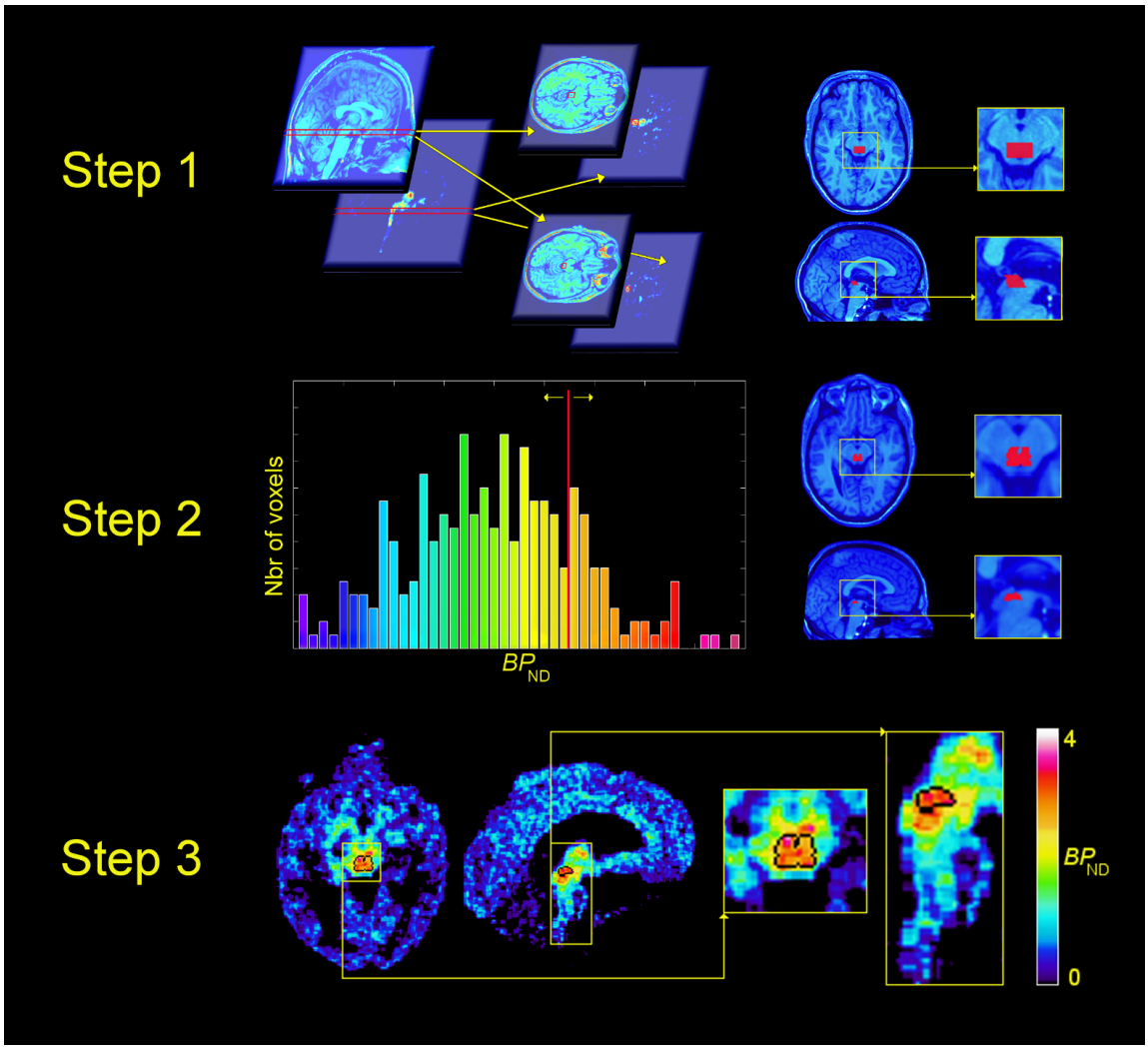

Figure 9. ROI delineation procedure for the raphe nuclei. *Step 1*, On coregistered MR images, top and bottom slices for each ROI were selected. Subsequently, a rectangle was drawn on the two slices such that the anatomical structure was well encapsulated within the intermediate volume between the top and the bottom rectangles. *Step 2*, The bounding box was eroded. Only those voxels for which the BP_{ND} value in the parametric image was higher than a predefined threshold (red line) constituted the final ROI. *Step 3*, The eroded ROIs were applied to the parametric PET images.

x_j of voxel i and voxel j,

$$M_{i,j} = \frac{\sum_{t=1}^{T}(x_i(t) - \bar{x}_i)(x_j(t) - \bar{x}_j)}{\sqrt{\sum_{t=1}^{T}(x_i(t) - \bar{x}_i)^2}\sqrt{\sum_{t=1}^{T}(x_j(t) - \bar{x}_j)^2}}, \tag{21}$$

where T denotes the number of time frames of the PET image.

The i:th row of M contains the correlation coefficients between voxel i and all other voxels in the image. Therefore, by selecting the rows corresponding to a few interesting voxels, all voxels correlating with the interesting voxels are identified. To limit the size of M, only those entries for which the corresponding voxel pairs displayed a strong measure of correlation ($|M_{i,j}| \geq \theta$ with $0 \leq \theta \leq 1$) were kept. In addition, to avoid extracting noisy voxels, all autocorrelations were manually zeroed (i.e., $M_{i,i} = 0$). This modification allows M to be represented as a sparse matrix, which is highly beneficial considering the

large number of voxels in the images. Once $\mathbf{M}$ is calculated, the selection of which rows to extract differs between the two applications.

3.8.2 PWC approach for image-derived input functions

PET images from the HRRT contain $\sim 14,000,000$ voxels. The number of elements in $\mathbf{M}$ is therefore $\sim 14,000,000^2$, which is a problematic matrix size even for a supercomputer to handle. For this application, an image subset was defined to reduce the computational load, containing only the neck region of the image (see figure 10). To identify all vox-

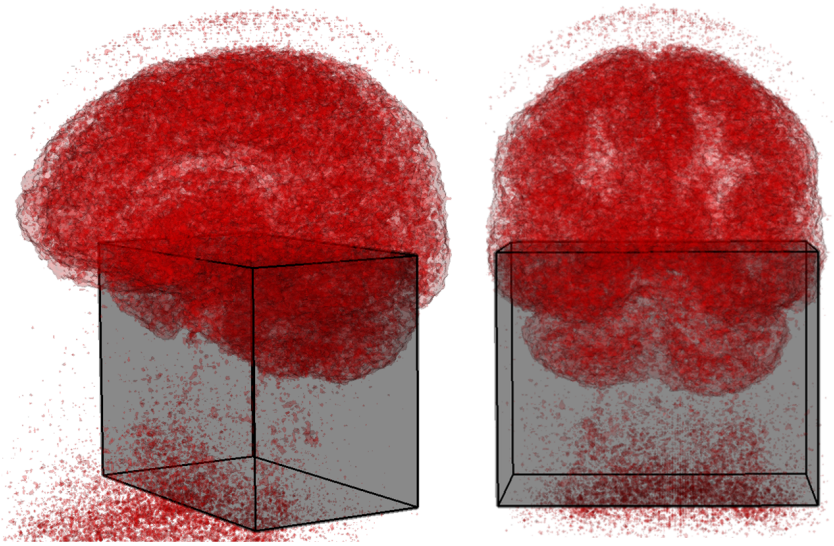

Figure 10. 3D-rendered summation PET image of one subject measured with [^{11}C]flumazenil. Gray box indicates the image subset used in the PWC algorithm to obtain image-derived input functions.

els within the subset displaying blood-like behavior, coregistered MR images were used. Since the signal from the carotid artery in MR images is very strong, the vessels can easily be segmented. At least a few of the carotid artery voxels identified from the segmented MRI are likely to display-blood like behavior, whereas others may display primarily noise. The noisy voxels will not correlate much with other voxels and therefore, will not affect the result. In contrast, the voxels with blood-like shape will correlate with all other voxels displaying blood-like behavior, which are identified as the entries in the rows of $\mathbf{M}$ corresponding to the artery voxels, with elements larger than 0. To identify all voxels with blood-like behavior, the rows of $\mathbf{M}$ corresponding to the voxels obtained from the segmented MRI were extracted and averaged into a single vector, where the i:th component contains the average correlation between voxel i, and all carotid artery voxels (as defined by the segmented MRI). The final carotid artery ROI was defined as all elements > 0 in that vector. The procedure described above is also illustrated in figure 11.

The carotid artery is a small, elongated structure with a diameter of approximately 5 mm [117]. The signal obtained from the cluster can therefore be assumed to be affected by substantial spill-out of radioactivity. The amount of spill-out from the ROI depends upon the radioactivity gradient between the vessel and the surrounding tissue, and thereby changes over the course of the measurement. A typical blood TAC consists of an early peak of radioactivity (approximately for $0 \leq t \leq 3$ minutes), followed by a long tail during which the radioactivity concentration in arterial blood is low and relatively unchanging.

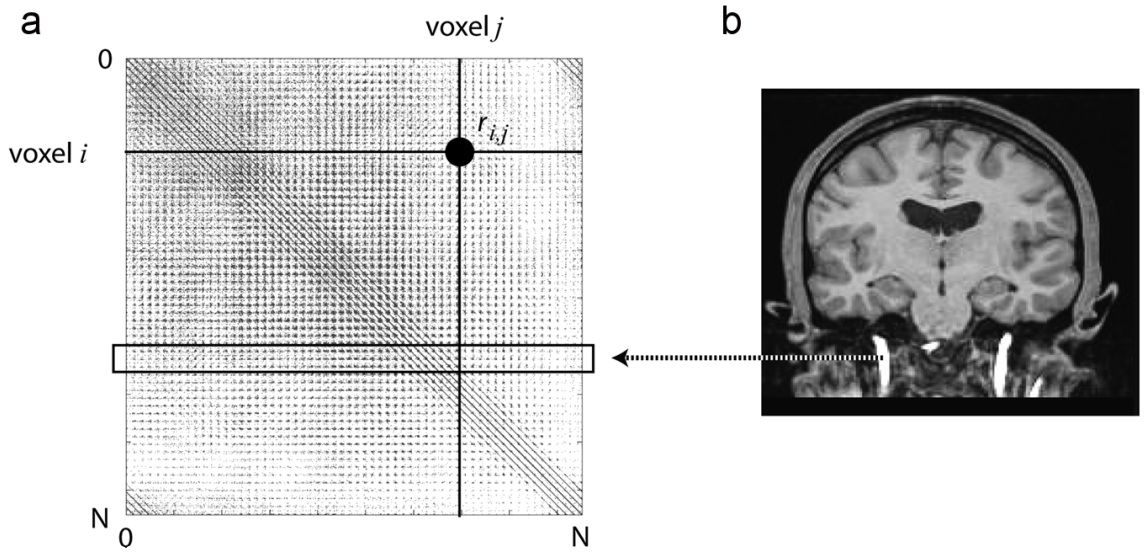

Figure 11. **a** Pearson product-moment correlation coefficient (PCC) between all voxel pairs in an image subset (number of voxels $N \sim 10^6$) stored in a sparse matrix $\mathbf{M}$. The PCC between the time-activity curves of voxels i and j is highlighted. **b** Carotid artery voxels were segmented from coregistered magnetic resonance (MR) images and used as indices to rows of $\mathbf{M}$ to extract correlated (columnar) voxels.

During the initial phase, when the bolus of radioactivity is still in the vessels, the gradient is large and substantial spill-out is expected. At later time points however, the gradient is much smaller and can potentially be neglected. Therefore, in this application, the first three minutes of the blood signal derived from the ROIs obtained from the PWC method were corrected for spill-out using a modified version the GTM method [48], The modification consist of reducing the number of compartments (or ROIs) to one. The TAC is thereby only corrected for spill-out of radioactivity, and contamination from the surrounding tissue to the vessel is neglected. The remaining part of the blood curve (the tail, $t > 3$ minutes) was scaled to the manually obtained blood samples.

3.8.3 PWC approach for amyloid clustering

In the general PWC approach described in section 3.8.1, regions or voxels can be used as seeds by extracting the rows of $\mathbf{M}$ that correspond to those voxels or regions. For estimation of image-derived input functions, the seeding region was defined as the carotid artery voxels obtained from segmented MR images. Similar approaches can of course be used in order to identify other types of networks of radioligand binding.

One potential application is to use the PWC approach to identify patterns of amyloid deposits. Although the deposition of amyloid plaques is widely distributed throughout the brain, the pattern of regional distribution may vary considerably across individuals. It has been shown that the pattern of regional distribution of amyloid-β affects the extent of cognitive decline, particularly if the pattern includes brain regions involved in memory encoding and decoding [155, 156]. If a pathological pattern of amyloid deposition characterizing the disease can be identified, it can facilitate differential diagnosis of AD. Below is a description of how the PWC approach was used to identify the pattern, and how the clusters were used to objectively discriminate between AD patients and controls subjects.

Identification of the patterns To test whether the above hypothesis was true, PET measurements from a total of 32 individuals (21 AD patients and 11 control subjects) were included. Rather than applying the PWC method on dynamic (4D) PET data, individual parametric images of BP_{ND} were used [40]. All individual (3D) parametric images were normalized to a common space (MNI) using SPM and stacked after each other along the fourth dimension, similar to what has been done for the serotonin and opioid systems [157]. In this way, each voxel displays a curve (or voxel curve) describing the interindividual variability of BP_{ND}. All pairwise correlations were then calculated between these voxel curves and stored in a sparse correlation matrix $\mathbf{M}$. Two different approaches for identifying the disease specific pattern were evaluated.

Clustering using a priori assumption Firstly, similar to what was done for the case of the image-derived input function, a seeding region was used to determine which rows in $\mathbf{M}$ to extract. The posterior cingulate cortex (PCC) has repeatedly been shown to, even at early stages of the disease, contain substantial amount of amyloid. By extracting all rows corresponding to a PCC ROI (manually defined using the Human Brain Atlas [153]), the voxels correlating with that region (implicitly, voxels correlating with amyloid) were identified. This method uses the a priori assumption that the PCC contains a high amyloid load and can be used as a seeding region. It is therefore referred to as the clustering procedure using an a priori assumption.

Clustering without a priori assumption For simplicity, let the stacked 3D parametric images be ordered so that the first N_{HC} images are from control subjects, and the remaining N_{AD} images are from AD patients. Then, all voxels affected by amyloid will display a "bump" in BP_{ND} in the transition between the groups. The size of the bump defines the "effect size" between the two groups, as illustrated in figure 12. The biological variability and random noise present in the images result in that voxels that display a non-zero effect size (i.e., voxels in which the AD group has a non-negligible load of amyloid) have a higher correlation to other amyloid-affected voxels, than the corresponding correlations among non-amyloid voxels as shown in figure 13 (please see the appendix of study V for a more thorough discussion). By identifying the voxels with the highest average correlation to other voxels, the voxels associated with a non-negligible effect size can be identified without any a priori assumption. In practice this was performed by setting a very high threshold θ for which entries to keep in $\mathbf{M}$, and then averaging all rows corresponding to brain tissue voxels. In the resulting vector, the i:th component corresponded to the average correlation between voxel i and all voxels for which that particular correlation was $\geq \theta$. The vector was then remapped to image space, where all voxels > 0 were set to 1, and constituted the final cluster.

Separation of amyloid positive from negative individuals The hypothesis in this project was that the identified clusters could improve the separation between amyloid positive and amyloid negative individuals. Two different separation approaches were evaluated for this purpose, either based on actual BP_{ND} values or on the spatial distribution of high amyloid-β voxels. Separation based on BP_{ND} values was simply performed by calculating the average BP_{ND} inside the cluster for each subject. Separation based on spatial agreement was more complex and was performed as follows.

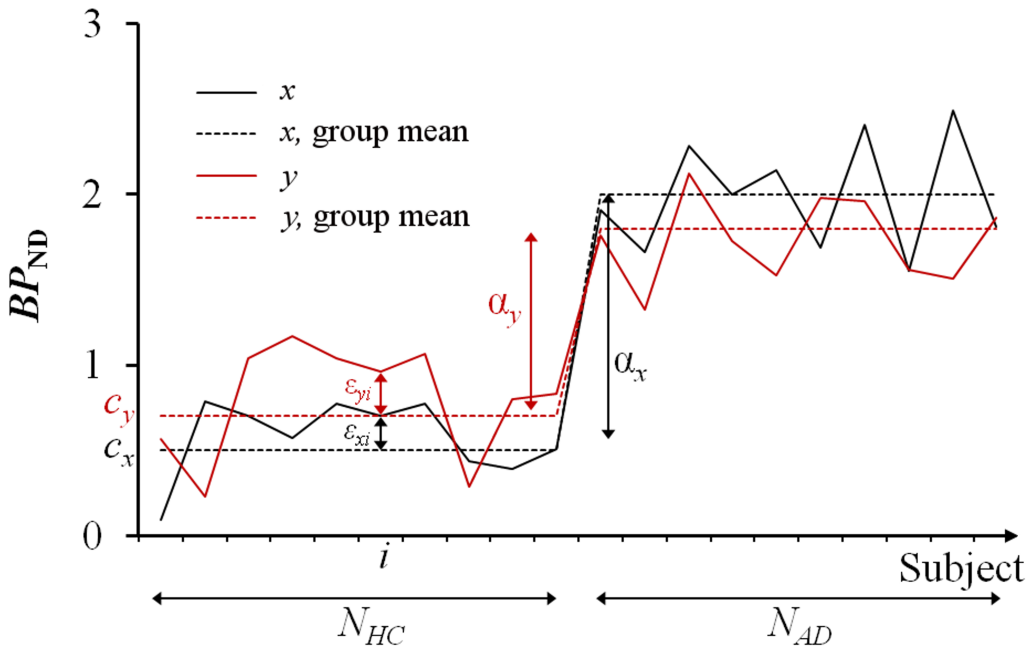

Figure 12. Illustration of two voxel curves x and y. The correlation between them will depend on their respective effect size α and noise levels ε.

First, the BP_{ND} values in each parametric image were normalized, so that the maximal voxel value was set to 100 and all other voxels were scaled accordingly. Second, the distribution of normalized BP_{ND} was visualized in a histogram and a threshold separating the AD group from the control subjects was identified. This threshold can be interpreted as "the value above which a voxel is considered a *high* BP_{ND} voxel, expressed as the percentage of the maximal BP_{ND} value for that subject". Consequently, for each subject, a set of the voxels was classified as high BP_{ND} voxels. The separation was then performed by comparing the spatial distribution of the high BP_{ND} voxels to the spatial distribution of the voxels included in the cluster. More specifically, the fraction of voxels in the cluster corresponding with high BP_{ND} voxels was calculated for each individual.

This study only encompasses AD patients and control subjects. For such individuals, the classifier should generate a large separation between the groups to minimize erroneous classifications and maximize the margins. To evaluate the performance of the classifier, a separation distance D between groups x and y was calculated as the distance between one SD below the average of the higher group and one SD above the average of the lower group, expressed as a fraction of the maximal range of the data, i.e.

$$D = \frac{(\bar{y} - \sigma_y) - (\bar{x} + \sigma_x)}{\max(y) - \min(x)}, \tag{22}$$

where $\bar{y} > \bar{x}$.

Can the method be applied to other disorders and biomarkers? With regard to the *Clustering without a priori assumptions* described above, an interesting question is whether the method can be applied to identify other types of pathological networks, with other effect sizes and studied with other radioligands. To assess the question, a simulation experiment

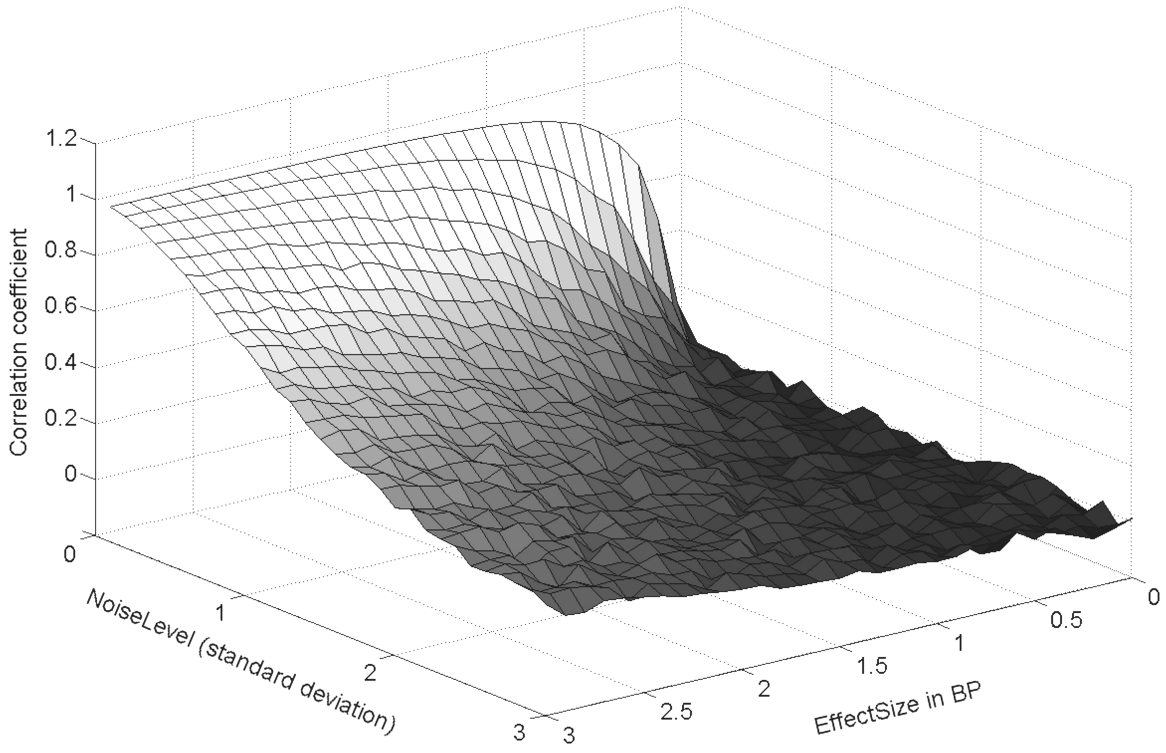

Figure 13. Calculation of the pearson product-moment correlation coefficient for a large number of voxel curves with different effect sizes and noise levels. Low noise levels and high effect sizes yield high correlations. Thus, by extracting the voxels with high correlations, the voxels with large effect sizes are identified.

was conducted, in which the voxel-wise connectivity was investigated under varying effect sizes and noise levels. Based on these simulated data, a *critical* effect size was established for each noise level. The critical effect size indicates the smallest possible effect size needed between patients and controls in order for the method to detect a connectivity pattern.

4 RESULTS AND DISCUSSION

4.1 Overview

In this thesis, several algorithms have been developed, implemented, and evaluated. The first study evaluated the difference in quantitative outcome measures between the HRRT and a lower resolution system, the HR system. In addition, the effect of correcting the data for PVE was investigated. In study II, a method to quantify radioligand binding in the small nuclei of the brainstem was developed, and evaluated using both HR and HRRT data. In study III, two automated methods for the definition of ROIs were evaluated, allowing for faster and more objective analysis of PET data. In study IV, a method to estimate the image-derived arterial input function was developed and validated. The performance of the method was compared to that of three previously published methods. Finally, in study V, the same method used in study IV was adapted and applied to PET measurements using radioligands that bind to amyloid-β, with the aim of classifying subjects based on their load of amyloid.

4.2 Section 1

4.2.1 Study I, Comparison of the HR and the HRRT PET systems

As described in section 1.4.2, the BP_{ND} values measured in the HRRT system should be higher than those obtained in the HR system due to higher resolution and lower PVE. Study I confirmed this notion for the frontal cortex and the whole GM. Although there was a trend towards higher binding potential measured with the HRRT in several of the other regions examined, the difference between the systems was not statistical significant (see figure 14). One possible explanation is that the effect of improved resolution is primarily manifested in rather small regions (see section 1.4.2 for more details). With the exception of the ventral midbrain and the dorsal brainstem, it is therefore possible that the ROIs included in study I were too large for the effect of improved resolution to become prominent. However, as described in section 1.4.3, traditional ROI-based quantification is not suitable for such small ROIs using the HRRT, due to the high voxel-to-voxel noise level. Thus, no statistically significant difference was observed in the ROIs for which we had anticipated a large difference between the systems. This observation became the motivation for study II.

The agreement between the systems increased after the data were corrected for PVE using the Meltzer and Müller-Gärtner methods. In particular, the very good agreement between the two systems was observed in cortical regions after correction with the Müller-Gärtner method (Figure 15). This increased agreement provides further support for the applicability of PVE correction techniques, since it can be assumed that the outcome measures from both systems were brought closer to the (unknown) true value. However, PVE correction introduces assumptions that should considered before the algorithms are applied. For instance, the Müller-Gärtner algorithm assumes that radioligand binding in the whole WM can be approximated by the average value obtained from an isolated portion of the centrum cemiovale. Violation of this assumption may lead to underestimation of binding in the WM portion of the subcortical regions, and thus underestimation of the contamination from WM to GM, and consequently resulting in an overcorrection of the data.

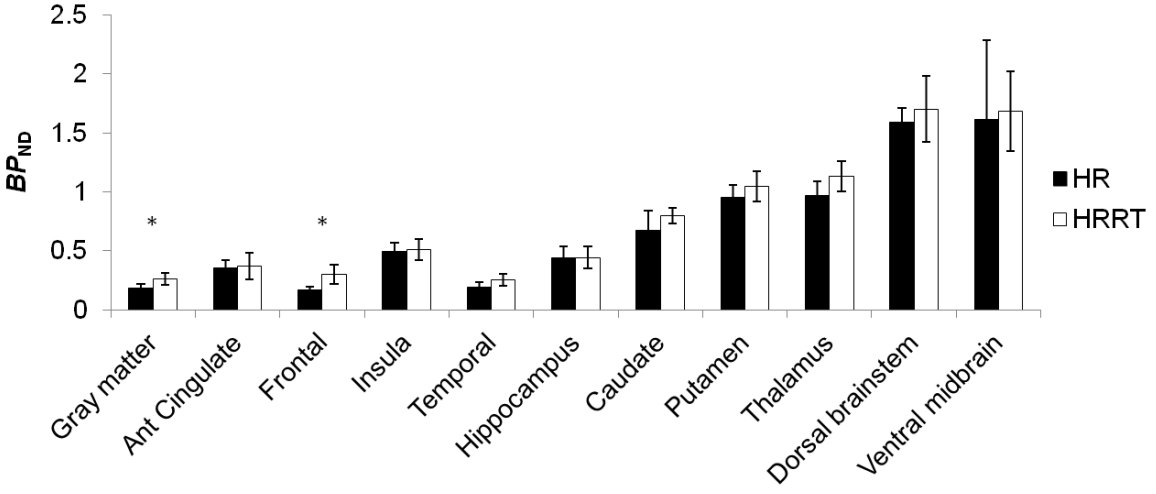

Figure 14. BP_{ND} measured in the HR and HRRT PET system for regions of different size and different 5-HTT density.

4.2.2 Study II, Measurement of serotonin transporter in the brainstem

To estimate the optimal parameter values for applying WAPI on HRRT data, regional BP_{ND} was estimated in one small and one large ROI using both WAPI and conventional ROI analysis (see section 3.7.1 for details). The parameter combination providing the best agreement between the two methods was selected for further analysis. The optimal parameter combination was found to be a filter kernel length value of 16 and a decomposition depth of 3, as shown in figure 16.

This parameter combination provided parametric images with high recovery and contrast. In particular, a clear visual difference was observed in the signal originating from raphe nuclei between the HR and the HRRT systems, as can be seen in figure 17. The semiautomatic ROI delineation procedure enabled definition of small and accurate ROIs for the superior colliculi, the ventral midbrain, the dorsal raphe nucleus, and the median raphe nucleus. For the more caudal raphe magnus and raphe obscurus, the BP_{ND} values were too low for the method to provide continuous ROIs. The two nuclei were therefore combined into a single caudal raphe ROI. The ROI delineation procedure is explained in section 3.7.2.

In each of the structures examined, the BP_{ND} estimated using the HRRT was significantly higher than the corresponding values obtained from the HR system. On average, the HRRT consistently provided approximately 30-40% higher BP_{ND} values than the HR, in all of the ROIs examined. In addition, the difference between the systems was not dependent on the threshold used in the ROI delineation procedure. An interesting question is whether it is possible to relate the difference in BP_{ND} between the two systems to measurements of their respective resolutions. One possibility is to assume that, for each structure examined, there exists a true, but unknown BP_{ND} value, and that the measured BP_{ND} value in each structure, ($BP_{\mathrm{ND}}^{\mathrm{HR}}$ and $BP_{\mathrm{ND}}^{\mathrm{HRRT}}$, respectively) is proportional to the true value multiplied by the recovery coefficient of the system,

$$\begin{cases} BP_{\mathrm{ND}}^{\mathrm{HR}} \propto BP_{\mathrm{ND}}^{\mathrm{true}} \cdot RC_{\mathrm{HR}} \\ BP_{\mathrm{ND}}^{\mathrm{HRRT}} \propto BP_{\mathrm{ND}}^{\mathrm{true}} \cdot RC_{\mathrm{HRRT}}^{PSF} \end{cases}, \tag{23}$$

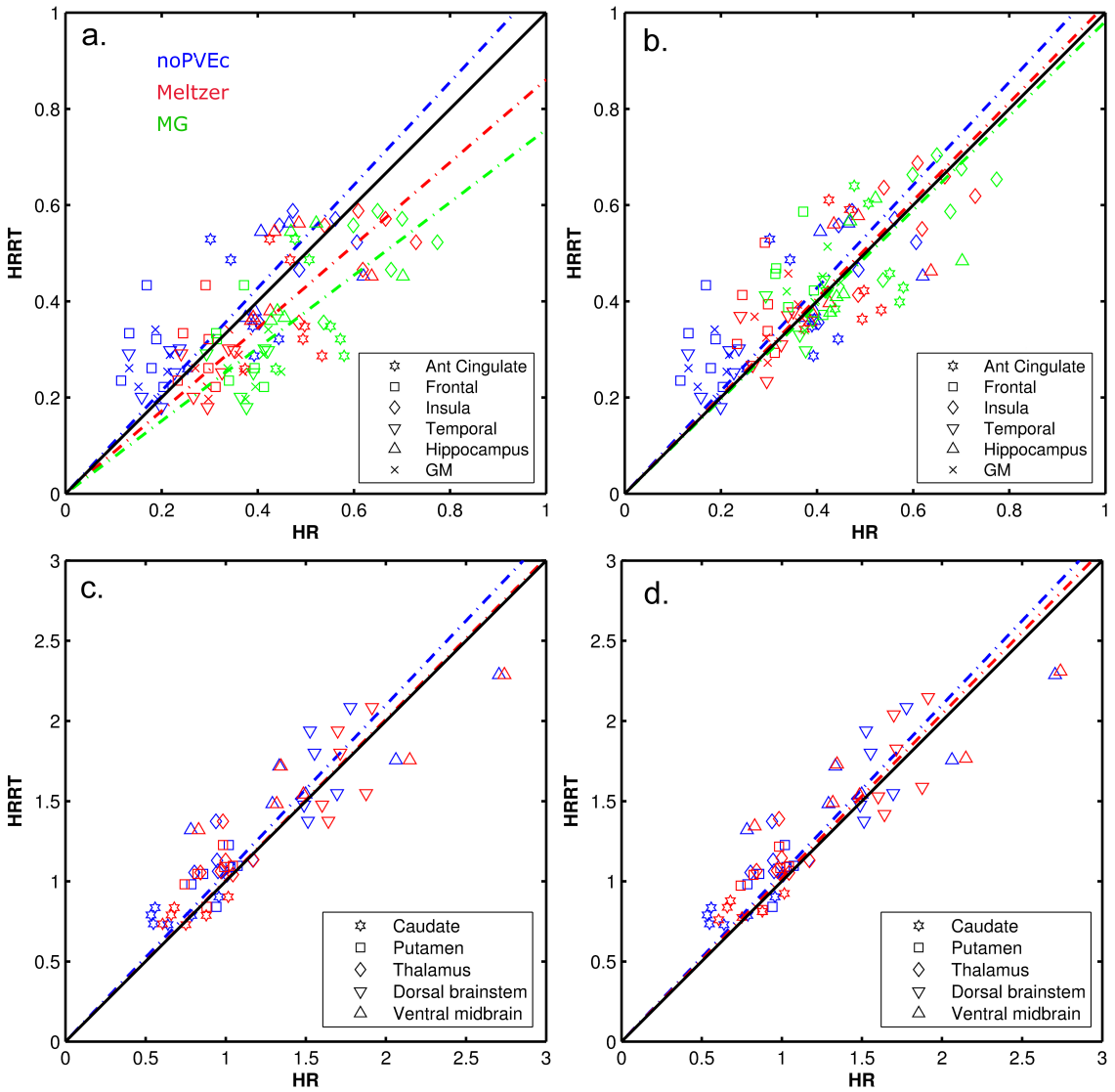

Figure 15. Scatterplot of BP_{ND} measured in the HR and HRRT before and after PVE correction. In **a** and **c**, only the HR data are corrected for PVE, whereas in **b** and **d**, both HR and HRRT data are corrected. Good agreement between the systems was found in cortical regions after the PVE correction approach proposed by Müller-Gärtner et al. was applied to both systems (**b**).

where RC denotes the recovery coefficient for each system. This assumption can be motivated by considering that $BP_{\mathrm{ND}} = DVR - 1$ and that the cerebellar TAC is rather unaffected by PVE. Since it is the same individual measured in both system, the unknown parameter $BP_{\mathrm{ND}}^{\mathrm{true}}$ can be substituted from equation 23. Rearrangement leads to

$$\frac{BP_{\mathrm{ND}}^{\mathrm{HR}}}{BP_{\mathrm{ND}}^{\mathrm{HRRT}}} = \frac{RC_{\mathrm{HR}}}{RC_{\mathrm{HRRT}}} \tag{24}$$

In a previous paper, Varrone et al. showed that the recovery coefficient for the HRRT system (including PSF modeling) was approximately 0.81 ($RC_{\mathrm{HRRT}}^{PSF} \approx 0.81$) in a 10 mm sphere [19]. To our knowledge similar measurements have not been performed for the HR system. The RC for its predecessor, the ECAT EXACT 922, has previously been estimated as 0.5 ($RC_{\mathrm{EXACT922}} \approx 0.5$) [158]. In addition, the recovery coefficient of the HRRT system *without* PSF-modeling has been estimated as 0.6 ($RC_{\mathrm{HRRT}}^{noPSF} \approx 0.6$) [19, 27]. It is

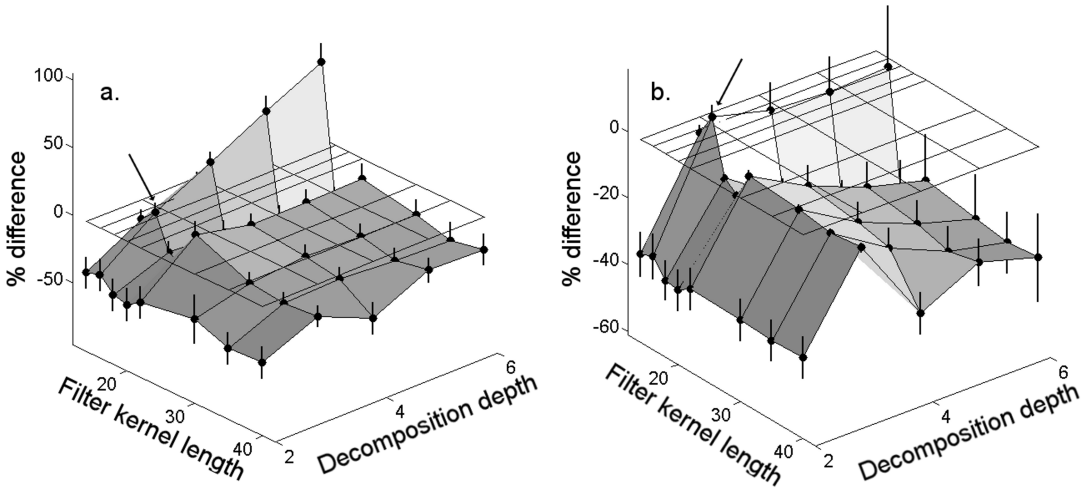

Figure 16. Percent difference between BP_{ND} estimated using graphical analysis and WAPI in (**a**) frontal and temporal cortices, and (**b**) dorsal brainstem. The transparent mesh illustrates identity between the two methods. The optimal combination of parameter values for the filter kernel length and decomposition depth was 16 and 3 (arrows).

reasonable to assume that

$$RC_{\mathrm{EXACT922}} \leq RC_{\mathrm{HR}} \leq RC_{\mathrm{HRRT}}^{noPSF}, \tag{25}$$

and thus, $0.5 \leq RC_{\mathrm{HR}} \leq 0.6$. Inserting this range of values for RC_{HR}, together with $RC_{\mathrm{HRRT}}^{PSF} \approx 0.81$ in the right hand side of equation 24, it is predicted that the ratio of BP_{ND} measured between the HR and the HRRT system should be ≈ 0.7. The corresponding ratios using the measured BP_{ND} values for each system were: 0.75 for the ventral midbrain, 0.74 for the superior colliculi, 0.73 for the dorsal raphe, 0.69 for the median raphe, and 0.74 for the caudal raphe. This agreement provides support for the notion that the dominating portion of the difference in BP_{ND} measured between the two systems are primarily caused by their disparate resolutions.

To conclude, the method in this study provided significantly higher BP_{ND} values for HRRT data than for HR data. The difference between the systems was not dependent on the threshold used to define the ROI. A relatively small intersubject variability in the estimates of BP_{ND} was obtained using this method. Altogether, it can be concluded that the method developed in this study allows for improved mapping and quantification of the density of 5-HTT in the brainstem.

4.3 Section 2

4.3.1 Study III, Evaluation of FreeSurfer and AAL for automatic delineation of ROIs

The purpose of study III was to evaluate the feasibility of using the AAL template and the FreeSurfer package to delineate ROIs for PET data analysis. Since manual delineation is considered the gold standard, regional outcome measures obtained using the automated methods for ROI delineation were compared to those obtained using manually delineated

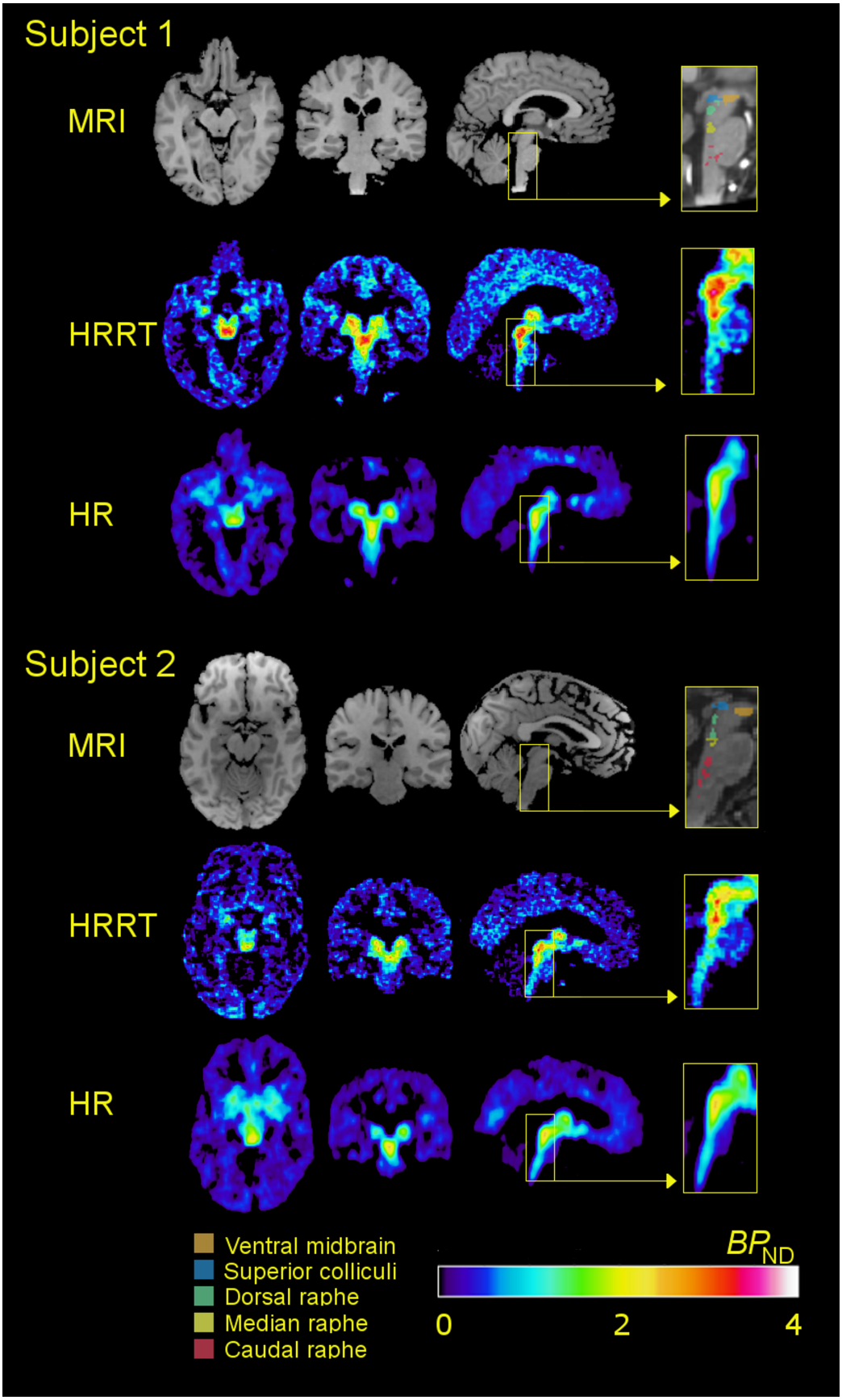

Figure 17. Parametric images of BP_{ND} using HR and HRRT data for two subjects. A distinct difference in recovery between the two systems is visible in the small 5-HTT-rich brainstem regions. For each subjects, the ROIs obtained from the semiautomatic ROI delineation procedure are superimposed on the T1-weighted MR images.

ROIs. The outcome measures used were BP_{ND} for [^{11}C]AZ10419369, and DVR for [^{11}C]AZD2184.

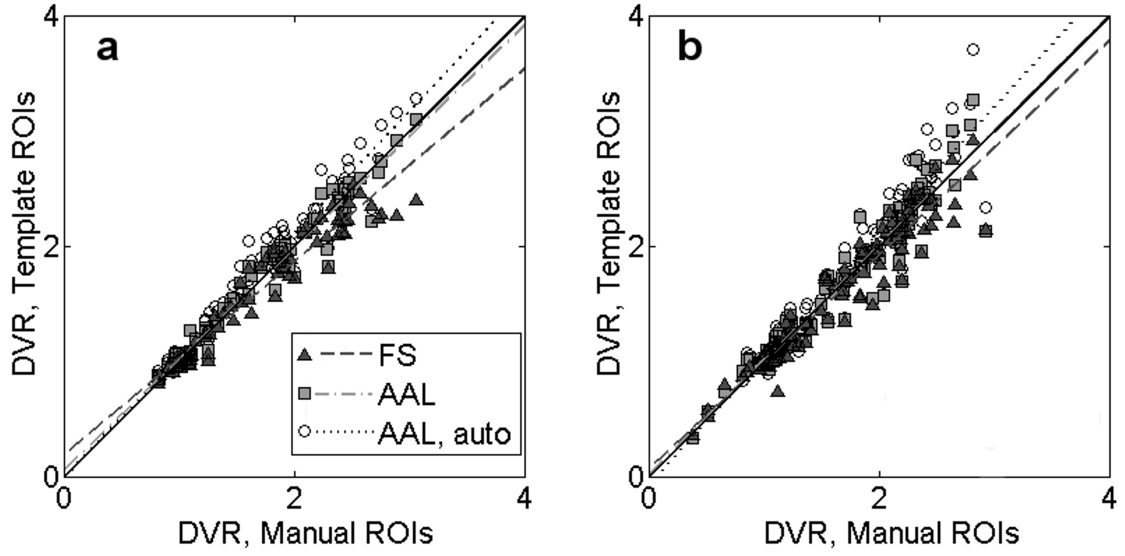

Figure 18. Scatter plot of DVR estimated with manual (x-axis) and automated (y-axis) ROIs for [^{11}C]AZD2184 data. **a**: HR, and **b**: HRRT data.

In general, the agreement in outcome measures between automated and manual ROIs was satisfactory. Figure 18 and 19 show the scatterplots between outcome measures obtained with automated and manual methods, for both HR and HRRT data. As shown in the figure, there is general agreement between the methods, but there are also some regions in which a substantial difference between outcome measures occurs.

The regions with a systematic difference between automated and manual ROIs include caudate nucleus, hippocampus, amygdala, posterior cingulate cortex, and dorsomedial prefrontal cortex. A general cause for the discrepancy between automated and manual ROIs is that the automated ROIs were significantly larger than the manually defined counterparts. As a consequence, the automated methods lack the buffer zones which are typically drawn by a manual rater, to avoid spill-over of radioactivity between the ROIs. The effect becomes prominent in regions adjacent to structures with high levels of radioligand binding. For instance, in the [^{11}C]AZ10419369 dataset, BP_{ND} values in amygdala and hippocampus were overestimated using automated ROIs. The amygdala is a small region located near basal forebrain structures that are associated with a high density of 5-HT$_{1\mathrm{B}}$ receptors [144], while the hippocampus is located adjacent to relatively high density structures such as pallidum. BP_{ND} estimated in these regions were consequently overestimated, possibly due to the lack of buffer zones.

Another interesting region to highlight is the caudate nucleus. BP_{ND} estimated in the caudate was systematically lower for both AAL and FreeSurfer than for the manual ROIs. The discrepancy between the automated and manual ROI for the caudate was primarily due to different anatomical definitions of the structure. The automated ROIs tended to cover the whole structure, whereas for the manually defined ROI of the caudate, only the ventrolateral part of the structure is traditionally drawn to avoid spill-out of radioactivity into the ventricles.

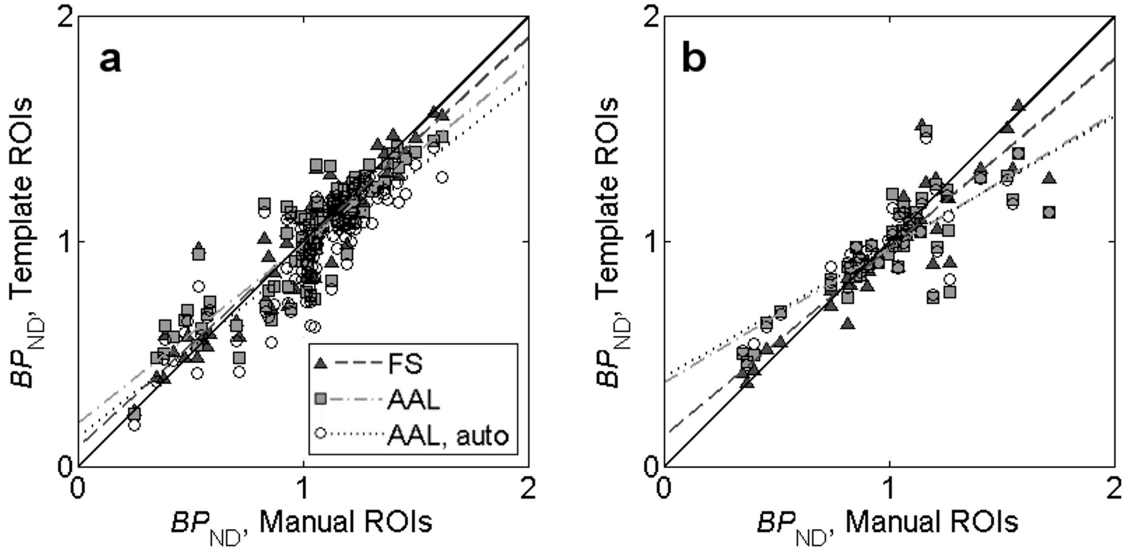

Figure 19. Scatter plot ofBP_{ND} estimated in manual (x-axis) and automated (y-axis) ROIs for [^{11}C]AZ10419369 data. **a**: HR, and **b**: HRRT data.

Is it possible to use an automatically defined reference region? A secondary aim of this study was to evaluate whether a modified version of the cerebellar ROI incorporated in AAL could be used as a reference region (similar evaluation was not performed for FreeSurfer since the cerebellar ROI in FreeSurfer deviated substantially from the manually defined version). The AAL cerebellar ROI was trimmed and cropped so that it resembled the manual counterpart as much as possible. Still, the outcome measures obtained using the automated reference region were consistently biased. Moreover, opposite biases was observed for the two radioligands; higher regional DVR was observed for [^{11}C]AZD2184 and lower BP_{ND} was observed for [^{11}C]AZ10419369. For [^{11}C]AZD2184, the larger automated cerebellum includes voxels close to the border of the fourth ventricle, and thus experiences a substantial spill-out of radioactivity. For [^{11}C]AZ10419369 however, this effect is compensated by the inclusion of the vascular tissue from the venous sinuses, which have been reported to have a high density of 5-HT$_{1\mathrm{B}}$ receptors [146]. The bias introduced by using the automatic reference region lowered the accuracy of the regional outcome measures. It can be concluded that, the AAL cerebellar ROI used in this study should not be used.

FreeSurfer or AAL? Despite the higher level of complexity of FreeSurfer, both methods showed similar accuracy in the estimates of regional outcome measures. The choice of which method to use is therefore dependent on other factors, such as the necessity of fast analysis as provided by the AAL template, or the need for anatomically detailed ROIs as provided by FreeSurfer. As a final remark, although it is not apparent from the data included in this study, FreeSurfer tended to provide more reliable segmentation of subcortical structures in subjects with severe atrophy than the AAL method, which in some cases included ventricular voxels in striatal ROIs.

4.4 Section 3

4.4.1 Study IV, Application of the pairwise correlation method to obtain image-derived arterial input function

In this study, the Pair-Wise correlation (PWC) method (see section 3.8) was applied to derive arterial input functions directly from PET images. For this purpose, 6 PET measurements acquired using the $GABA_A$ radioligand [^{11}C]flumazenil, and 6 measurements acquired using the 5-HT_{1B} receptor radioligand [^{11}C]AZ10419369 were used. The performance of the PWC method was compared to that of Chen's method [108], Mourik's method [110], and Naganawa's method [113]. The PWC method enabled identification of voxels

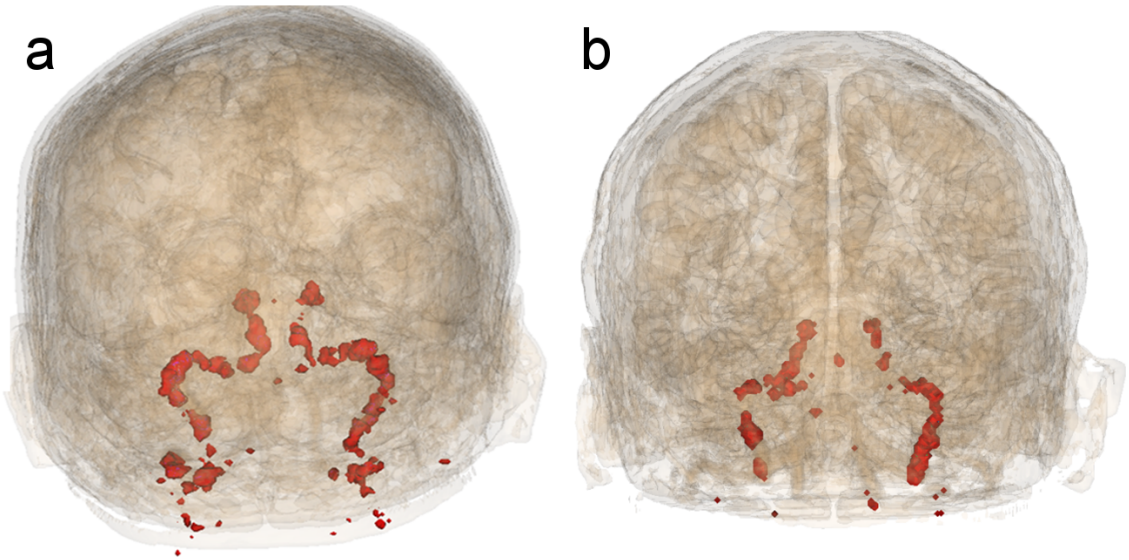

Figure 20. Clusters derived from two representative subjects using the PWC method in order to identify voxels with blood-like behavior. **a**: [^{11}C]flumazenil, and **b**: [^{11}C]AZ10419369.

displaying blood-like behavior for all subjects. Two representative clusters are shown in figure 20. Applying the clusters to the dynamic PET measurements together with the correction scheme (i.e., correcting the first 3 minutes for spill-out of radioactivity using the Rousset method reduced to one compartment and tail scaling to the remaining part of the curve) provided blood curves which were in good agreement to the measured radioactivity levels in arterial blood. Consequently, the regional V_T values obtained using the PWC method were well matched to those obtained using the measured arterial input function. Using the PWC method, the percent difference was on average $\sim 3\%$.

As can be seen in figure 21, the performance of the PWC method was similar to or better than the other three methods in terms of its ability to generate V_T values similar to the measured input functions. Naganawa's method, which is based on independent component analysis (ICA), provided blood curves with negative values for all subjects measured with [^{11}C]flumazenil and provided high variability in the estimates for V_T of [^{11}C]AZ10419369. Considering the complex nature of ICA, it is likely that Naganawa's method could perform better if it were tuned for each radioligand used [159]. In this study however, the method was applied as described in the original publication [113].

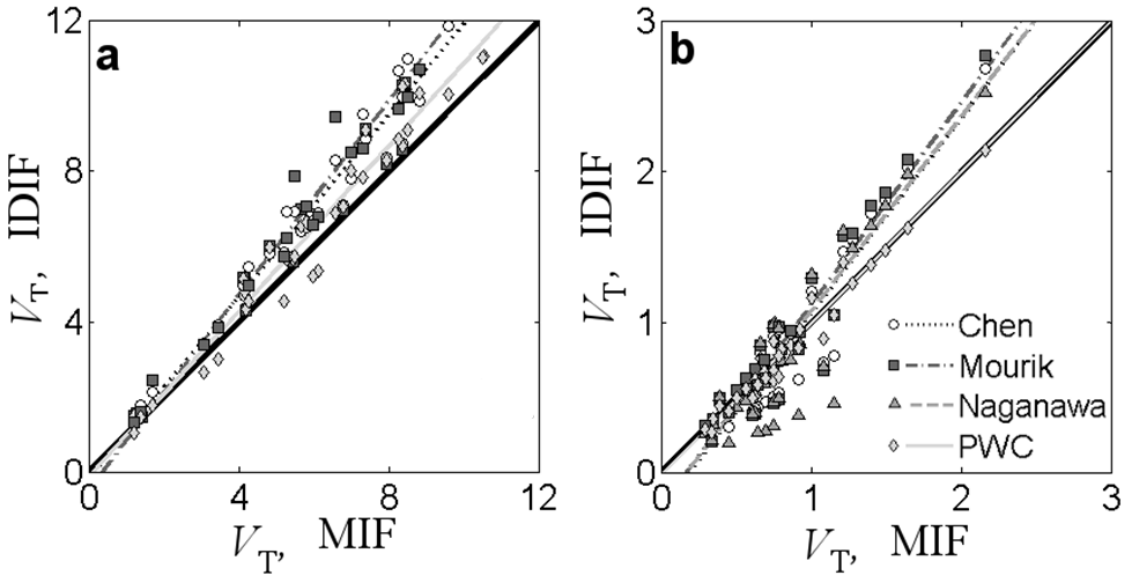

Figure 21. Scatter plot showing the agreement between V_T obtained using image-derived input functions (x-axis) versus measured input functions y-axis for **a**: [^{11}C]flumazenil, and **b**: [^{11}C]AZ10419369. Note that V_T derived using Naganawa's method is not included in **a**, since it provided IDIFs with negative values for all subjects measured with [^{11}C]flumazenil. For both radioligands, V_T derived using the PWC provided slopes closer to 1 and intercepts closer to 0.

Mourik's and Chen's methods both overestimated regional V_T values in the subjects measured with [^{11}C]flumazenil by approximately 20% (corresponding value using the PWC method was 7%). This overestimate probably results from the fact that both Chen's and Mourik's methods only take the initial part of the measurement into account when defining the carotid ROI, allowing for inclusion of voxels affected by noise in the late part of the measurement.

In this study, the Logan plot was used to estimate regional V_T-values (see description in 1.3.6). This introduces some limitations in the interpretations of the results. In the Logan method, calculation of V_T is based on the AUC of the input functions, and is less sensitive to erroneously estimated initial peaks. All of the methods evaluated in this study displayed some variability in the estimates of the peak radioactivity. However, this variability is to some extent suppressed in the estimates of regional V_T-values. The early peak of the blood curve primarily affects the rate of influx of radioactivity across the blood-brain barrier, which is reflected by the rate constant K_1. Uncertainty in the estimate of the peak signal may therefore introduce an uncertainty in the estimates of K_1. Thus, the methods evaluated in this thesis should be used with caution in situations where changes in blood flow are expected.

There are other consequences of using quantification methods which emphasizes the AUC of the input function. In this study, the [^{11}C]flumazenil dataset showed worse performance for the Chen's, Mourik's, and the PWC method as compared to [^{11}C]AZ10419369. Interestingly, the [^{11}C]flumazenil also showed significantly lower AUC of the standardized uptake value of the input functions than [^{11}C]AZ10419369 datasets ($p = 8.2 \cdot 10^{-4}$, two-tailed t-test). Thus, for [^{11}C]flumazenil, small fluctuations in the input functions represent a larger proportion of the total AUC than for [^{11}C]AZ10419369, which makes V_T obtained from IDIF more sensitive to noise and to other factors affecting the image quality (such as

the image reconstruction settings).

As a final remark, although it seems likely that the PWC method would work for a larger array of radioligands, it needs to be evaluated for each one separately. For example, radioligands such as [^{11}C]MADAM and [^{11}C]DASB, which bind to the serotonin transporter, might provide low signal from the blood due to the prevalence of 5-HTT in lung tissue and to the large distribution volume in the body. Thus, the carotid-to-background ratio is reduced, making the signal from blood hard to distinguish from tissue signal. To our knowledge, no method for extracting IDIF has been shown to work for these radioligands, possibly due to low signal-to-noise ratio.

4.4.2 Study V, Application of the pairwise correlation method to cluster voxels with amyloid

In this study, it was hypothesized that the PWC method could be applied to identify a disease specific spatial pattern of amyloid, which characterizes the distribution of radioligand binding in a group of AD patients. This disease specific pattern, or cluster, was identified by investigating how the voxels correlated across a group consisting of 10 AD patients and 6 controls examined with [^{18}F]AZD4694. More specifically, two different approaches to define the cluster were evaluated. The first approach was based upon the assumption that in AD patients the posterior cingulate cortex (PCC) contains a high level of amyloid. Thus, all voxels correlating with the voxels in the PCC were identified. The resulting cluster is shown in figure 22a. The voxels identified were located in regions which have previously been shown to be affected by amyloid in traditional ROI-based analysis.

Using PCC as a seeding region is a valid approach for the present purpose. However, the use of a seeding region introduces methodological limitations. For other applications, it is possible that no suitable seeding region, i.e., a brain region displaying the known signal of interest, can be identified. Therefore we also investigated the possibility of identifying the disease specific amyloid pattern without any a priori assumptions. Voxels experiencing an effect size between the patients and controls correlate with other voxels displaying a non-zero effect size. Due to the presence of noise and biological variability in the data, the correlation coefficient between voxels with effect size is higher than the correlation coefficients between voxels without effect size. In other words, the correlation coefficient between two amyloid voxels will be higher than the correlation coefficient between two non-amyloid voxels (a more thorough discussion on this matter is given in the appendix of study V). Thus, by finding the voxels that have a high average correlation coefficient to other voxels, the amyloid voxels are identified without the need of a seeding region. The cluster obtained in this manner is shown in figure 22b.

The voxels included in these clusters reflect the spatial distribution characterizing AD, and can thus be used to create a classifier that clearly separates patients from controls. The classification can for instance be based on calculating the average BP_{ND} inside the cluster for each individual. Using this approach and the clusters shown in figure 22 for the PET images acquired with [^{18}F]AZD4694 and an additional dataset consisting of 16 PET images acquired with [^{11}C]AZD2184, we found complete separation between controls and AD patients as shown in figure 23a and b. For both clusters, the separation distance (equation 22) was approximately 30% for the [^{18}F]AZD4694 and 50% for the [^{11}C]AZD2184 datasets.

Although the AD group in general has higher BP_{ND} values than the control sub-

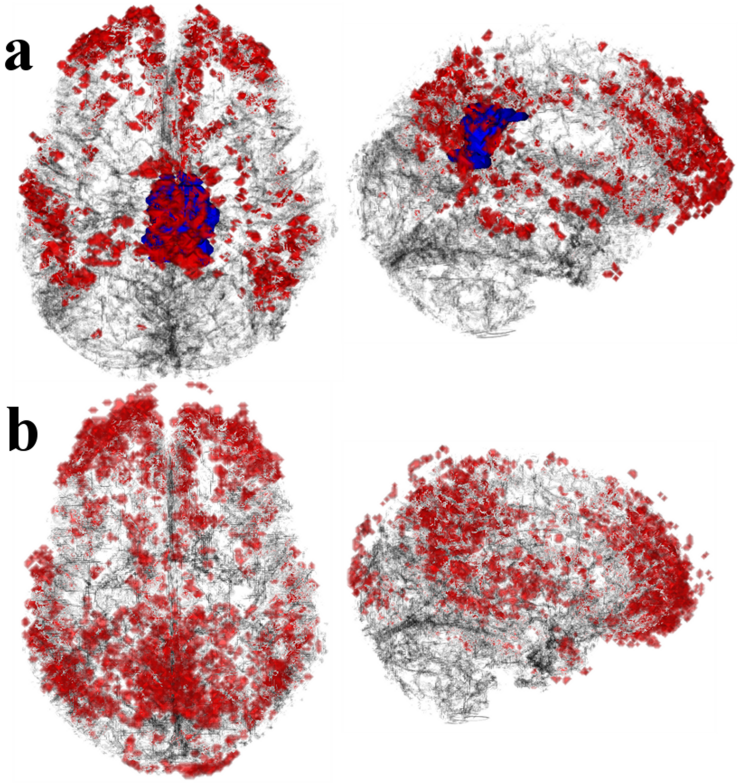

Figure 22. Clusters of amyloid obtained using the PWC approach. **a**: Posterior cingulate cortex (blue) was used as a seeding region, and **b**: the voxels having the highest average correlation to other voxels (i.e., no seeding region).

jects, interindividual differences in the actual BP_{ND} values are expected. These differences can cause overlaps between AD patients and healthy individuals who have low but non-negligible levels of amyloid concentration [138–140]. Rather than measuring the actual BP_{ND}, an interesting alternative is to compare the individual spatial distribution of the voxels affected by a high amyloid load to the spatial distribution of the voxels assumed to characterize the disease (i.e., the clusters in figure 22). The separation between the groups obtained using this approach is shown in figure 24, and the corresponding separation distance was approximately 50% and 70% for the [^{18}F]AZD4694 and the [^{11}C]AZD2184 datasets, respectively.

The two methods described above provided a convincing separation distance between the AD patients and the control subjects. This large separation distance suggests that the measurement is restricted to the regions in the brain which are found to characterize the disease. Furthermore, focusing the classifier on the spatial distribution of amyloid rather than the actual BP_{ND} values provided a substantial increase in the separation between the groups. Consequently, the spatial distribution of amyloid is a more powerful measurement for group separation. This becomes particularly interesting when considering that a distinct pattern of amyloid has been shown to affect the extent of cognitive decline. These observations provide further support for the theory that it is not amyloid per se that characterizes AD, but rather, amyloid in certain vulnerable brain regions. These brain regions do not necessarily adhere to the conventional definition of brain regions, and thus, the separation is improved when conventional ROIs are not used.

So far, this method has only been applied to a group of healthy subjects and AD

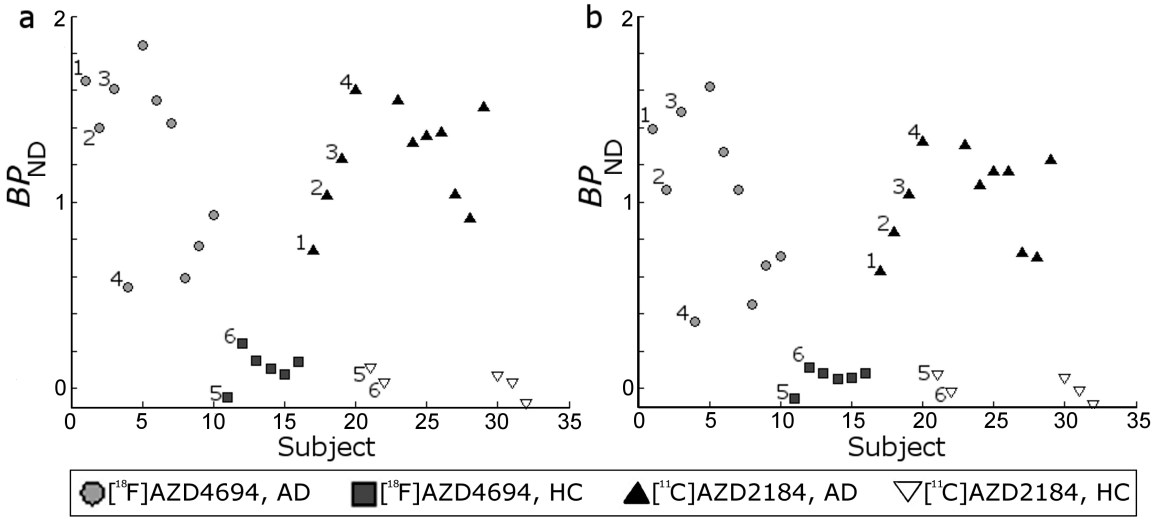

Figure 23. Separation of individuals based on the average BP_{ND} inside the clusters obtained **a**: using PCC as a seeding region, and **b**: without seeding region.

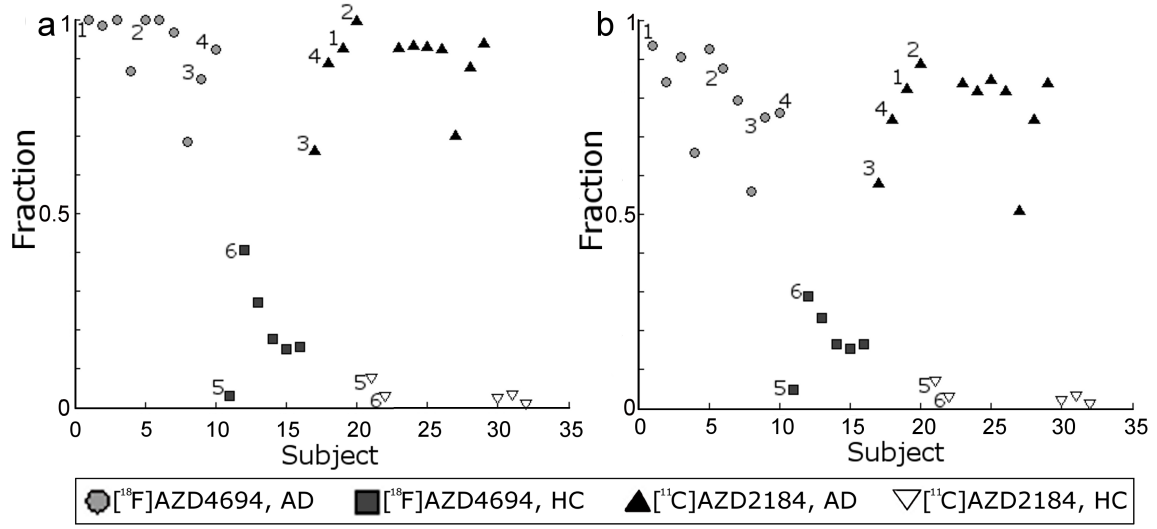

Figure 24. Separation of individuals based on the spatial similarity between the distribution of high BP_{ND} voxels and the clusters, obtained **a**: using PCC as a seeding region, and **b**: without seeding region.

patients. Its predictive accuracy on subjects having prodromal stages of AD is therefore not assessed. Still, increased separation distance at least reduces the risk of misclassifying patients associated with low amyloid signal as healthy. In addition, since the formation of amyloid plaques appears to follow a rather well-characterized spatial pattern as the disease progresses, it is possible that the cluster is gradually filled by high BP_{ND} voxels. If this is true, *intermediately* filled cluster (e.g., subjects in between the two extremes shown in figure 24) may be interpreted as an indicator for progression towards onset of AD, and thus serve as a marker for being at risk of developing the disease.

Can the method be applied to other disorders and biomarkers? The *Clustering without a priori assumptions* method relies on the assumption that correlations among voxels showing only background signal will be lower than correlations among voxels associated with the specific signal, due to the presence of noise and biological variability in the data. In a simulation experiment, the correlation coefficient between a large number of voxel curves with different effect sizes and noise levels was calculated. For each voxel, the average correlation to other voxels is shown in figure 25 for three different values of θ. In figure 25, a unique combination of effect size and noise level is assigned to each small square (or "scenario", 20×20 pixels). All scenarios correspond to an effect size > 0, and thus each scenario corresponds to a pathological state. If > 95% of the pixels in a scenario were correctly classified as displaying a "disease specific" signal, the corresponding condition (i.e., effect size and noise level) was considered "manageable". All scenarios associated with manageable conditions are marked in white in the right column of figure 25.

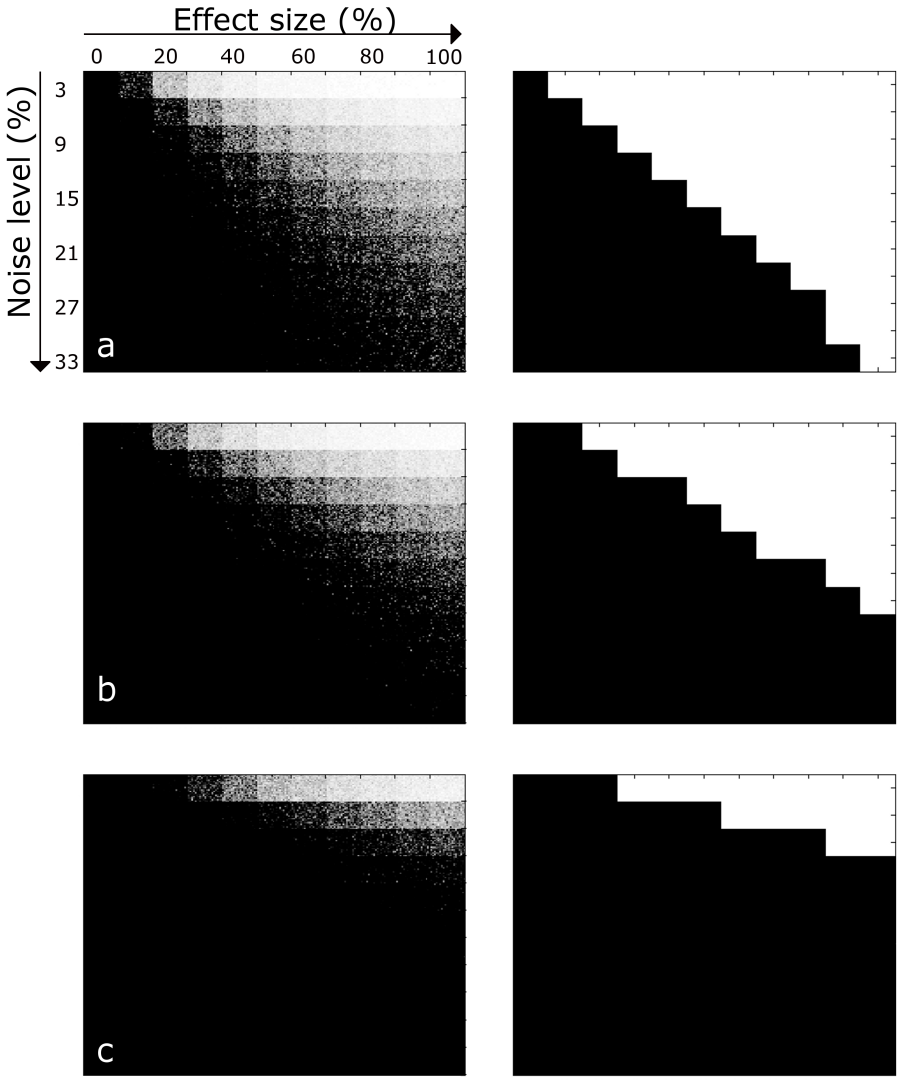

Figure 25. Results from the simulation showing the voxels displaying high average correlation to other voxels, for various effect sizes and noise levels. **a**: $\theta = 0.90$, **b**: $\theta = 0.95$, and **c**: $\theta = 0.985$.

The simulation illustrates that it is possible to derive a cluster without using a seeding region, if the effect size is larger than a critical value, which in turn depends on the value

of θ. However, suitable values for θ are decided by the size of $\mathbf{M}$, and cannot be predicted in advance. Thus it is not straight-forward to predict the performance of the method when applied to other radioligands and biomarkers. Nevertheless, for each noise level, there exists a critical effect size below which the algorithm will not work. Although the simulation experiment suggests that the method can be generalized, the performance of the method applied in situations with suitable noise levels and effect sizes remains to be elucidated.

5 CONCLUSIONS

The focus of this thesis has been on methodological advancements of PET data quantification. The findings are summarized below.

5.1 Section 1

- The higher resolution of the HRRT as compared to the HR system is to some extent reflected in the higher outcome measures. Correcting the data for partial volume effects increases the agreement between the systems.
- In the small brainstem regions, we expected that the difference between binding potential estimated in the two systems would be substantial. Instead we found no difference between the systems and a high intersubject variability. This unexpected finding probably results from the high noise levels of the HRRT which prevent accurate measurement of radioligand binding using conventional ROI-based analysis.
- Wavelet-aided parametric imaging, in combination with HRRT, can provide images with suppressed noise levels and with sufficient resolution to accurately resolve small brainstem structures. This procedure, when used with a semi automatic method to derive small brainstem ROIs, enabled detailed mapping of serotonin transporter density in several small brainstem structures. This procedure provides more robust estimates of BP_{ND} than conventional ROI-based analysis. In addition, the difference in BP_{ND} between the HR and HRRT PET systems was significant and mainly attributable to their disparate resolutions.

5.2 Section 2

- Both the AAL and FreeSurfer can be used to automatically delineate ROIs for the quantification of PET data obtained using the two radioligands [^{11}C]AZD2184 and [^{11}C]AZ10419369.
- Since the performances of AAL and FreeSurfer are similar, the choice of the method can be based on other situational factors, such as the need for short processing time as provided by AAL, or the need for more detailed ROIs as provided by FreeSurfer.

5.3 Section 3

- The pairwise correlation approach can be used to define ROIs for the carotid arteries, using the radioligands [^{11}C]flumazenil and [^{11}C]AZ10419369. After applying the PWC method, compensating for spill-out of radioactivity, and applying tail-scaling, the image-derived arterial input functions were in good agreement with the measured input functions.
- The developed method performed similarly or better than three previously suggested methods, published by Chen et al., Mourik et al., and Naganawa et al.
- The PWC method can also be applied to cluster voxels associated with amyloid load. When the PWC method was applied to a group of AD patients and healthy controls, a

common pattern of amyloid-β was identified, either by using the posterior cingulate cortex as a seeding region or by finding the voxels with the highest connectivity to other voxels.

- The PWC method is generic and can likely be successfully applied to other radioligands and biomarkers.

6 FUTURE PERSPECTIVES

High resolution PET imaging or hybrid systems? During recent years, there has been a trend towards building hybrid systems such as PET/MR [160–162]. A hybrid system is in theory the best of two worlds; high resolution MR images provide detailed structural information, and high sensitivity PET images provide the ability to accurately quantify radiotracer distribution. However, the hybrid systems developed so far for human brain imaging have resolutions comparable to that of the HR system [161] because modifications in instrumentation are required for the two modalities to be integrable. The results in study I suggest that no major implications on conventional ROI-based analysis are to be expected from this reduction in resolution. However, the results of study II indicate that accurate quantification of small brain structures, such as the raphe nuclei, might not be possible using the lower resolution hybrid systems. Since the raphe nuclei are not clearly detectable on MR images, hybrid systems provide limited value for that particular application.

Quantifying radioligand concentration in small brain structures. The methodology for quantification of radioligand binding in the small brainstem nuclei described in study II is limited by the volumetric assumption regarding the volume of the nucleus. For healthy individuals, the assumption may well be valid, but not for patients with expected neurodegeneration, such as patients with Parkinson's disease. A potential workaround is to use the proposed method to generate an ROI-template for the brainstem in a generic space and then spatially warp it to parametric images of the patients. Although particular attention needs to be paid to the spatial normalization, the procedure may enable quantification of serotonin transporter in the brainstem of both patients and healthy subjects.

Automated or manual ROIs in the future? Continuous improvements in image registration and segmentation algorithms are expected, which will implicitly also improve the accuracy of template-based methods for definitions of ROIs. The future of PET applied to neurological sciences are likely not to include any manually defined ROIs at all, considering the undisputable benefits associated with automated methods. In the years to come, publications utilizing a large amount of pooled PET data quantified using automated ROIs can be expected, similar to the recently published work by Savli et al. [163] including $\sim$100 PET measurements. Using PET image databases of such proportions, many interesting biological findings can be anticipated.

Correction for PVE in the future. With the introduction of automated methods for ROI definition, a more routine use of the Rousset PVE-correction scheme can be anticipated in the near future. Theoretically, the smaller the ROIs, the weaker is the assumption regarding homogeneous binding inside the ROI. The extreme case is to apply the correction to individual voxels rather than ROIs. Such procedure would allow for using PSFs with increased FWHM for voxel close to the edges to account for the varying resolution in the FOV. Although the method is today too computationally demanding, it may well be a versatile option in the future.

Image-derived input function – challenges and opportunities. Numerous methods to estimate the image-derived input function have been suggested. Alternatives to complex

methods to estimate the IDIF are population-based input functions [164] and simultaneously estimated input functions, i.e., methods simultaneously estimating the parameters of the input function and the rate constants of several brain regions [165]. Unfortunately, the PET system cannot distinguish between radioactivity concentration from the parent radioligand and its metabolites. Blood samples are therefore still needed even for a perfect method of estimating the IDIF. Using blood samples for scaling the blood curve is not necessarily a drawback of the method, since the data will be available anyway. Still, the invasiveness can be reduced if venous samples can be used for scaling rather than arterial samples. An interesting alternative is to predict the arterial radioligand concentration based on venous measurements [166], similarly to what has been done for nicotine studies [167].

Amyloid clustering. In general, with increased computational power and memory capacities, more voxel-based multivariate statistical analysis of PET data for improved diagnosis of AD can be anticipated. Combining cognitive tests and various biomarkers have previously been shown to improve the prediction rate of AD [168], and thus we can expect more studies including both amyloid PET, as well as volumetric measurements of the hippocampus and concentration of amyloid-β in CSF. The methodology described in study V has the benefit that such external parameters can be easily incorporated, by simply extending the matrix by one row and column per measure.

7 ACKNOWLEDGEMENTS

This thesis is the result of 4 incredible years of doctorate studies, through which I have had the opportunity to meet and collaborate with so many talented people. I would like to specially thank a few people whom I have had the pleasure to have close contact with during past years:

First, my main supervisor Associate Professor Andrea Varrone, for the invaluable support, mentorship, scientific guidance, enthusiasm, and the dedication you have shown. Also, thank you for the loyalty and thoughtfulness, and, most of all, thank you for believing in me.

My co-supervisor Professor Lars Farde for valuable scientific input, interesting discussions and thorough writing tutorials. Professor Anders Lansner, my co-supervisor, for dedicating the time and resources required for the fruitful collaboration between KI and KTH. Professor Christer Halldin for all the optimism and encouragement shown over the years, and Professor Balazs Gulyás for interesting scientific discussions.

Karin Zahir, the hub around which the PET center revolves, for all your help. Your dedication makes the life of a PhD student so much easier! Dr Katarina Varnäs for great collaboration, for providing valuable feedback on the thesis, for interesting discussions, and, most of all, for being a wonderful roommate.

Miklós Tóth, my brother in arms, for unquestioned loyalty and friendship. Dr Anton Forsberg for great scientific collaboration and for the numerous fun discussions. Dr Pavitra Kannan for your enthusiasm and encouragement, and for your amazing proof-reading of the thesis (was that comma right?). Dr Magdalena Nord for your care and for being a dedicated mentor and a good friend. Dr Simon Benjaminsson for a fruitful collaboration and for your unbreakable optimism.

I would also like to acknowledge the Knights of the Round Table on the 0'th floor: Pontus Plavén Sigray and Granville Matheson for hilarious discussions and valuable (?) insights, Dr Karin Collste, Dr Pauliina Ikonen, and Dr Mikael Tiger for interesting discussions and good laughs, Dr Shigeyuki Yamamoto, Dr Marie Svedberg, Dr Janine Doordin, Kalman Nagy, Roman Krais, Lenke Tari, Björn Wolbert, Sara Lundqvist and Matteo Ferrante for your great company, Dr Patrik Fazio for your optimism and sound perspectives, Dr Jenny Häggkvist for your friendship and solid encouragement, it really made a difference!

Dr Johan Lundberg, Dr Akihiro Takano, and Dr Sjoerd Finnema for your in-depth knowledge and your willingness to explain, and Dr Simon Cervenka, for PhD and career-related advice and for being a sound board for ideas.

All the current and past research nurses of the PET group, including Karin Olsson, Nina Knave, Anncathrin Kallin, Gudrun Nylen, Pia Schönbeck and Sophia Sjödin. A special thank you is also directed to Urban Hansson, Göran Rosenqvist, and Nils Sjöholm for logistic help and valuable scientific discussions.

The Astra Zeneca personnel, especially, Dr Magnus Schou and Dr Zsolt Cselényi for many valuable and educative discussions, and Ewa Lindström-Böö and Carina Jägenstedt Bismut for all the help retrieving the ethical documentation for the data from Astra studies.

All current and former colleagues at the PET center for making the work environment more enjoyable, Mahabuba Jahan , Sangram Nag, Kenneth Dahl, Dr Nahid Amini, Nándor Kaposy, Vladimir Stepanov, Anna Sumic, Carsten Steiger, Guennadi Jogolev, Jacqueline Borg, Linda Bergman, Hanna Hallenberg, Jan Andersson, Per Stenkrona, Stefan Borg, Arsalan Amir, Julio Gabriel, Yoko Ikoma, Peter Johnström, Aurelija Jucaite, Patrik Mattson,

Andreas Vestermark, Ryuji Nakao, Dr Fabienne Gourand, Hanna Jacobson Ingemyr, Dr Raisa Krasikova, Henrik Alfredéen, Jacob Kihlström, Kai-Chun Yang, Martina Sjöström, Obaidur Rahman, Siv Eriksson, Stefan Martinsson, Zhisheng Jia, and Zsolt Sarnyai.

I would also like to acknowledge my IRL friends simply for being such an adorable crew. Especially, thank you Erik for valuable help with the stress management.

A special thank you goes to my beloved family, Yvonne, Bengt, Ulla, Jona, Helena, Robert, Ebba, Oscar, Göte, Marie, Ulrika, Pelle, Saga, and Lukas, and in particular, my brother Mattias for your invaluable support and encouragement. And lastly, Carola, my love, thank you for your endless and uncompromised love and for showing me that love is bigger than chemical reactions in the brain.

8 REFERENCES

[1] Roobottom, C. A., Mitchell, G. & Morgan-Hughes, G. Radiation-reduction strategies in cardiac computed tomographic angiography. *Clin Radiol* **65**, 859–67 (2010).

[2] Nagy, B., Farmer, J. D., Bui, Q. M. & Trancik, J. E. Statistical basis for predicting technological progress. *PLoS One* **8** (2013).

[3] Morrocchi, M. *et al.* Proof of concept of an imaging system demonstrator for PET applications with SiPM. *Nucl Instrum Meth A* **720**, 67–69 (2013).

[4] Yoshida, E. *et al.* The X'tal cube PET detector with a monolithic crystal processed by the 3D sub-surface laser engraving technique: Performance comparison with glued crystal elements. *Nucl Instrum Meth A* **723**, 83–88 (2013).

[5] Bieniosek, M. F., Olcott, P. D. & Levin, C. S. Compact pulse width modulation circuitry for silicon photomultiplier readout. *Phys Med Biol* **58** (2013).

[6] Angelis, G. I. and Reader, A. J. and Markiewicz, P. J. and Kotasidis, F. A. and Lionheart, W. R. and Matthews, J. C. Acceleration of image-based resolution modelling reconstruction using an expectation maximization nested algorithm. *Phys Med Biol* **58** (2013).

[7] Schmidt, J. *et al.* Interpreting PET scans by structured patient data: a data mining case study in dementia research. *Knowl Inf Syst* **24**, 149–170 (2010).

[8] Schreibmann, E., Waller, A. F., Crocker, I., Curran, W. & Fox, T. Voxel clustering for quantifying pet-based treatment response assessment. *Med Phys* **40** (2013).

[9] Prainsack, B. & Buyx, A. A solidarity-based approach to the governance of research biobanks. *Med L Rev* **21**, 71–91 (2013).

[10] Ozel, D., Bilge, U., Zayim, N. & Cengiz, M. A web-based intensive care clinical decision support system: From design to evaluation. *Inform Health Soc CA* **38**, 79–92 (2013).

[11] Jeffery, R., Iserman, E. & Haynes, R. B. Can computerized clinical decision support systems improve diabetes management? A systematic review and meta-analysis. *Diabetic Med* **30**, 739–745 (2013).

[12] Mosconi, L., De Santi, S., Rusinek, H., Convit, A. & de Leon, M. J. Magnetic resonance and PET studies in the early diagnosis of Alzheimer's disease. *Expert Rev Neurother* **4**, 831–49 (2004).

[13] Savitz, J., Lucki, I. & Drevets, W. C. 5-HT(1A) receptor function in major depressive disorder. *Prog Neurobiol* **88**, 17–31 (2009).

[14] Rajah, M. N. & D'Esposito, M. Region-specific changes in prefrontal function with age: a review of PET and fMRI studies on working and episodic memory. *Brain* **128**, 1964–83 (2005).

[15] Cervenka, S., Backman, L., Cselenyi, Z., Halldin, C. & Farde, L. Associations between dopamine D2-receptor binding and cognitive performance indicate functional compartmentalization of the human striatum. *NeuroImage* **40**, 1287–95 (2008).

[16] Varnas, K., Varrone, A. & Farde, L. Modeling of PET data in CNS drug discovery and development. *J Pharmacokinet Pharmacodyn* **40**, 267–79 (2013).

[17] Moses, W. W. Fundamental Limits of Spatial Resolution in PET. *Nucl Instrum Methods Phys Res A* **648 Supplement 1**, S236–S240 (2011).

[18] Aleisso, A. & Kinahan, P. E. PET Image Reconstruction. In Henkin, R. (ed.) *Nuclear Medicine* (Mosby, 2006), 2 edn.

[19] Varrone, A. *et al.* Advancement in PET quantification using 3D-OP-OSEM point spread function reconstruction with the HRRT. *Eur J Nucl Med Mol Imaging* **36**, 1639–50 (2009).

[20] Phelps, M. E., Hoffman, E., Huang, S. C. & M.M, T.-P. Effect of positron range on spatial resolution. *J Nucl Med - Instrumentation and physics* **16**, 649–652 (1975).

[21] Levin, C. S. & Hoffman, E. J. Calculation of positron range and its effect on the fundamental limit of positron emission tomography system spatial resolution. *Phys Med Biol* **44**, 781–99 (1999).

[22] Champion, C. & Le Loirec, C. Positron follow-up in liquid water: II. Spatial and energetic study for the most important radioisotopes used in PET. *Phys Med Biol* **52**, 6605–6625 (2007).

[23] Champion, C., Le Loirec, C. & Stosic, B. EPOTRAN: a full-differential Monte Carlo code for electron and positron transport in liquid and gaseous water. *Int J Radiat Biol* **88**, 54–61 (2012).

[24] DeBendetti, S., Cowan, C., Konneker, W. & Primakoff, H. On the angular distribution of two-photon annihilation radiation. *Phys Rev* **77**, 205–212 (1950).

[25] Colombino, P., Fiscella, B. & Trossi, L. Study of positronium in water and ice from 22 to -144°C by annihilation quanta measurements. *Nuovo Cimento* **38**, 707–723 (1965).

[26] Shibuya, K. *et al.* Annihilation photon acollinearity in PET: volunteer and phantom FDG studies. *Phys Med Biol* **52**, 5249–61 (2007).

[27] de Jong, H. W. *et al.* Performance evaluation of the ECAT HRRT: an LSO-LYSO double layer high resolution, high sensitivity scanner. *Phys Med Biol* **52**, 1505–26 (2007).

[28] Adam, L. E., Karp, J. & Brix, G. Monte Carlo simulation of the scatter contribution in a 3D whole-body PET. *IEEE Nucl. Sci. Symp* **3**, 1969–1975 (1998).

[29] Cherry, S. R. & Huang, S. C. Effects of scatter on model parameter estimates in 3D PET studies of the human brain. *IEEE Trans Nucl Sci* **42**, 1174–1179 (1995).

[30] Watson, C. C., Newport, D. & Casey, M. E. A single scatter simulation technique for scatter correction in 3D PET. In Grangeat, P. & Amans, J. (eds.) *Three-Dimensional Image Reconstruction in Radiology and Nuclear Medicine*, vol. 4 of *Computational Imaging and Vision*, 255–268 (Kluwer Academic Publishers, Grenoble, 1996).

[31] Derenzo, S. E., Moses, W. W., Huesman, R. H. & Budinger, T. F. Critical instrumentation issues for ≤ 2 mm resolution, high sensitivity brain PET. In Uemura, K. (ed.) *Quantification of Brain Function: Tracer Kinetics and Image analysis in Brain PET*, 25–37 (Elsevier Science & Technology Books, Amsterdam, 1993).

[32] Carson, R. Tracer Kinetic Modeling in PET. In Bailey, D., Townsend, D., Valk, P. & Maisey, M. (eds.) *Positron emission tomography: Basic Science and Clinical Practice*, 382 (Springer Verlag, London, 2003), 1 edn.

[33] Innis, R. B. *et al.* Consensus nomenclature for in vivo imaging of reversibly binding radioligands. *J Cereb Blood Flow Metab* **27**, 1533–9 (2007).

[34] Logan, J. *et al.* Graphical analysis of reversible radioligand binding from time-activity measurements applied to [N-11C-methyl]-(-)-cocaine PET studies in human subjects. *J Cereb Blood Flow Metab* **10**, 740–7 (1990).

[35] Mintun, M. A., Raichle, M. E., Kilbourn, M. R., Wooten, G. F. & Welch, M. J. A quantitative model for the in vivo assessment of drug binding sites with positron emission tomography. *Ann Neurol* **15**, 217–27 (1984).

[36] Lammertsma, A. A. *et al.* Comparison of methods for analysis of clinical [11C]raclopride studies. *J Cereb Blood Flow Metab* **16**, 42–52 (1996).

[37] Lammertsma, A. A. & Hume, S. P. Simplified reference tissue model for PET receptor studies. *NeuroImage* **4**, 153–8 (1996).

[38] Logan, J. *et al.* Distribution volume ratios without blood sampling from graphical analysis of PET data. *J Cereb Blood Flow Metab* **16**, 834–40 (1996).

[39] Gunn, R. N., Lammertsma, A. A., Hume, S. P. & Cunningham, V. J. Parametric imaging of ligand-receptor binding in PET using a simplified reference region model. *NeuroImage* **6**, 279–87 (1997).

[40] Cselenyi, Z., Olsson, H., Farde, L. & Gulyas, B. Wavelet-aided parametric mapping of cerebral dopamine D2 receptors using the high affinity PET radioligand [11C]FLB 457. *NeuroImage* **17**, 47–60 (2002).

[41] Wienhard, K. *et al.* The ECAT EXACT HR: performance of a new high resolution positron scanner. *J Comput Assist Tomogr* **18**, 110–8 (1994).

[42] Wienhard, K. *et al.* Evaluation of a new high resolution research tomograph: The ECAT HRRT. *J Nucl Med* **43**, 227p–227p (2002).

[43] Eriksson, L. *et al.* Phoswich solutions for the PET DOI problem. *Nucl Instrum Meth A* **648**, S288–S292 (2011).

[44] Comtat, C. *et al.* Image based resolution modeling for the HRRT OSEM reconstructions software. In *2008 IEEE Nuclear Science Symposium and Medical Imaging Conference*, IEEE Nuclear Science Symposium - Conference Record, 3395–3398 (2009).

[45] Sureau, F. C. *et al.* Impact of image-space resolution modeling for studies with the high-resolution research tomograph. *J Nucl Med* **49**, 1000–8 (2008).

[46] Meltzer, C. C., Leal, J. P., Mayberg, H. S., Wagner, J., H. N. & Frost, J. J. Correction of PET data for partial volume effects in human cerebral cortex by MR imaging. *J Comput Assist Tomogr* **14**, 561–70 (1990).

[47] Muller-Gartner, H. W. *et al.* Measurement of radiotracer concentration in brain gray matter using positron emission tomography: MRI-based correction for partial volume effects. *J Cereb Blood Flow Metab* **12**, 571–83 (1992).

[48] Rousset, O. G., Ma, Y. & Evans, A. C. Correction for partial volume effects in PET: principle and validation. *J Nucl Med* **39**, 904–11 (1998).

[49] Slifstein, M. *et al.* Measurement of Partial Volume Effect in the ventral striatum using [11C]Raclopride. In Senda, M., Kimura, Y. & Herscovitch, P. (eds.) *Brain Imaging Using PET*, vol. 1, 123–127 (Academic Press, Amsterdam, 2002), 1 edn.

[50] Du, Y., Tsui, B. M. & Frey, E. C. Partial volume effect compensation for quantitative brain SPECT imaging. *IEEE Trans Med Imaging* **24**, 969–76 (2005).

[51] Kim, E. *et al.* Partial volume correction using structural-functional synergistic resolution recovery: comparison with geometric transfer matrix method. *J Cereb Blood Flow Metab* **33**, 914–20 (2013).

[52] Meltzer, C. C. *et al.* Comparative evaluation of MR-based partial-volume correction schemes for PET. *J Nucl Med* **40**, 2053–65 (1999).

[53] Teo, B. K. *et al.* Partial-volume correction in PET: validation of an iterative postreconstruction method with phantom and patient data. *J Nucl Med* **48**, 802–10 (2007).

[54] Tohka, J. & Reilhac, A. Deconvolution-based partial volume correction in Raclopride-PET and Monte Carlo comparison to MR-based method. *Neuroimage* **39**, 1570–84 (2008).

[55] Thomas, B. A. *et al.* The importance of appropriate partial volume correction for PET quantification in Alzheimer's disease. *Eur J Nucl Med Mol Imaging* **38**, 1104–19 (2011).

[56] Boussion, N. *et al.* A multiresolution image based approach for correction of partial volume effects in emission tomography. *Phys Med Biol* **51**, 1857–76 (2006).

[57] Boussion, N., Cheze Le Rest, C., Hatt, M. & Visvikis, D. Incorporation of wavelet-based denoising in iterative deconvolution for partial volume correction in whole-body PET imaging. *Eur J Nucl Med Mol Imaging* **36**, 1064–75 (2009).

[58] Erlandsson, K., Buvat, I., Pretorius, P. H., Thomas, B. A. & Hutton, B. F. A review of partial volume correction techniques for emission tomography and their applications in neurology, cardiology and oncology. *Phys Med Biol* **57**, R119–59 (2012).

[59] Young, S. N. & Leyton, M. The role of serotonin in human mood and social interaction. Insight from altered tryptophan levels. *Pharmacol Biochem Behav* **71**, 857–65 (2002).

[60] Meneses, A. 5-HT system and cognition. *Neurosci Biobehav Rev* **23**, 1111–25 (1999).

[61] Cryan, J. F., Harkin, A., Naughton, M., Kelly, J. P. & Leonard, B. E. Characterization of D-fenfluramine-induced hypothermia: evidence for multiple sites of action. *Eur J Pharmacol* **390**, 275–85 (2000).

[62] Ursin, R. Serotonin and sleep. *Sleep Med Rev* **6**, 55–69 (2002).

[63] Roberts, M. H. 5-Hydroxytryptamine and antinociception. *Neuropharmacology* **23**, 1529–36 (1984).

[64] Hornung, J. P. The human raphe nuclei and the serotonergic system. *J Chem Neuroanat* **26**, 331–43 (2003).

[65] Hornung, J. Raphe Nuclei. In Paxinos, K. J., G. (ed.) *The Human Nervous System*, 424–448 (Elsevier Academic Press, San Diego, 2004), second edn.

[66] Yeung, L. Y., Kung, H. F. & Yew, D. T. Localization of 5-HT1A and 5-HT2A positive cells in the brainstems of control age-matched and Alzheimer individuals. *Age (Dordr)* **32**, 483–95 (2010).

[67] Zhang, X., Andren, P. E., Greengard, P. & Svenningsson, P. Evidence for a role of the 5-HT1B receptor and its adaptor protein, p11, in L-DOPA treatment of an animal model of Parkinsonism. *Proc Natl Acad Sci U S A* **105**, 2163–8 (2008).

[68] Svenningsson, P. *et al.* Alterations in 5-HT1B receptor function by p11 in depression-like states. *Science* **311**, 77–80 (2006).

[69] Underwood, M. D. *et al.* Morphometry of the dorsal raphe nucleus serotonergic neurons in suicide victims. *Biol Psychiatry* **46**, 473–83 (1999).

[70] Halliday, G. M., Blumbergs, P. C., Cotton, R. G., Blessing, W. W. & Geffen, L. B. Loss of brainstem serotonin- and substance P-containing neurons in Parkinson's disease. *Brain Res* **510**, 104–7 (1990).

[71] Leroy, C. *et al.* Assessment of 11C-PE2I binding to the neuronal dopamine transporter in humans with the high-spatial-resolution PET scanner HRRT. *J Nucl Med* **48**, 538–46 (2007).

[72] Halldin, C. *et al.* [11C]MADAM, a new serotonin transporter radioligand characterized in the monkey brain by PET. *Synapse* **58**, 173–83 (2005).

[73] Cselenyi, Z., Olsson, H., Halldin, C., Gulyas, B. & Farde, L. A comparison of recent parametric neuroreceptor mapping approaches based on measurements with the high affinity PET radioligands [11C]FLB 457 and [11C]WAY 100635. *NeuroImage* **32**, 1690–708 (2006).

[74] Savitz, J. B. & Drevets, W. C. Neuroreceptor imaging in depression. *Neurobiol Dis* 49–65 (2012).

[75] Tzourio-Mazoyer, N. *et al.* Automated anatomical labeling of activations in SPM using a macroscopic anatomical parcellation of the MNI MRI single-subject brain. *NeuroImage* **15**, 273–89 (2002).

[76] Fischl, B. *et al.* Sequence-independent segmentation of magnetic resonance images. *Neuroimage* **23 Suppl 1**, S69–84 (2004).

[77] Collins, D. L. *et al.* Design and construction of a realistic digital brain phantom. *IEEE Trans Med Imaging* **17**, 463–8 (1998).

[78] Desikan, R. S. *et al.* An automated labeling system for subdividing the human cerebral cortex on MRI scans into gyral based regions of interest. *NeuroImage* **31**, 968 – 980 (2006).

[79] Fischl, B. *et al.* Automatically Parcellating the Human Cerebral Cortex. *Cereb Cortex* **14**, 11–22 (2004).

[80] Fischl, B. *et al.* Sequence-independent segmentation of magnetic resonance images. *NeuroImage* **23**, S69 – S84 (2004).

[81] Fischl, B. & Dale, A. M. Measuring the thickness of the human cerebral cortex from magnetic resonance images. *P Natl Acad Sci USA* **97**, 11050–11055 (2000).

[82] Fischl, B., Liu, A. & Dale, A. M. Automated manifold surgery: constructing geometrically accurate and topologically correct models of the human cerebral cortex. *IEEE Medical Imaging* **20**, 70–80 (2001).

[83] Fischl, B. *et al.* Whole brain segmentation: automated labeling of neuroanatomical structures in the human brain. *Neuron* **33**, 341–355 (2002).

[84] Fischl, B., Sereno, M. I., Tootell, R. B. & Dale, A. M. High-resolution intersubject averaging and a coordinate system for the cortical surface. *Hum Brain Mapp* **8**, 272–284 (1999).

[85] Jovicich, J. *et al.* Reliability in multi-site structural MRI studies: Effects of gradient non-linearity correction on phantom and human data. *NeuroImage* **30**, 436 – 443 (2006).

[86] Kuperberg, G. R. *et al.* Regionally localized thinning of the cerebral cortex in Schizophrenia. *Arch Gen Psychiat* **60**, 878–888 (2003).

[87] Rosas, H. D. *et al.* Regional and progressive thinning of the cortical ribbon in Huntington's disease. *Neurology* **58**, 695–701 (2002).

[88] Salat, D. *et al.* Thinning of the cerebral cortex in aging. *Cereb Cortex* **14**, 721–730 (2004).

[89] Segonne, F. *et al.* A hybrid approach to the skull stripping problem in MRI. *NeuroImage* **22**, 1060 – 1075 (2004).

[90] Dale, A., Fischl, B. & Sereno, M. I. Cortical Surface-Based Analysis: I. Segmentation and Surface Reconstruction. *NeuroImage* **9**, 179 – 194 (1999).

[91] Fischl, B., Sereno, M. I. & Dale, A. Cortical Surface-Based Analysis: II: Inflation, Flattening, and a Surface-Based Coordinate System. *NeuroImage* **9**, 195 – 207 (1999).

[92] Han, X. *et al.* Reliability of MRI-derived measurements of human cerebral cortical thickness: The effects of field strength, scanner upgrade and manufacturer. *NeuroImage* **32**, 180–194 (2006).

[93] Sled, J., Zijdenbos, A. & Evans, A. A nonparametric method for automatic correction of intensity nonuniformity in MRI data. *IEEE Trans Med Imaging* **17**, 87–97 (1998).

[94] Segonne, F., Pacheco, J. & Fischl, B. Geometrically accurate topology-correction of cortical surfaces using nonseparating loops. *IEEE Trans Med Imaging* **26**, 518–529 (2007).

[95] Reuter, M., Rosas, H. D. & Fischl, B. Highly Accurate Inverse Consistent Registration: A Robust Approach. *NeuroImage* **53**, 1181–1196 (2010).

[96] Reuter, M. & Fischl, B. Avoiding Asymmetry-Induced Bias in Longitudinal Image Processing. *NeuroImage* **57**, 19–21 (2011).

[97] Reuter, M., Schmansky, N. J., Rosas, H. D. & Fischl, B. Within-subject template estimation for unbiased longitudinal image analysis". *NeuroImage* **61**, 1402–1418 (2012).

[98] Gronenschild, E. H. *et al.* The effects of FreeSurfer version, workstation type, and Macintosh operating system version on anatomical volume and cortical thickness measurements. *PLoS One* **7**, e38234 (2012).

[99] Lehmann, M. *et al.* Atrophy patterns in Alzheimer's disease and semantic dementia: a comparison of FreeSurfer and manual volumetric measurements. *NeuroImage* **49**, 2264–74 (2010).

[100] Chen, B. C. *et al.* A new noninvasive quantification of renal blood flow with N-13 ammonia, dynamic positron emission tomography, and a two-compartment model. *J Am Soc Nephrol* **3**, 1295–306 (1992).

[101] Litton, J. E. Input function in PET brain studies using MR-defined arteries. *J Comput Assist Tomogr* **21**, 907–9 (1997).

[102] Su, K. H., Wu, L. C., Liu, R. S., Wang, S. J. & Chen, J. C. Quantification method in [18F]fluorodeoxyglucose brain positron emission tomography using independent component analysis. *Nucl Med Commun* **26**, 995–1004 (2005).

[103] Parker, B. J. & Feng, D. G. Graph-based Mumford-Shah segmentation of dynamic PET with application to input function estimation. *IEEE Trans Nucl Sci* **52**, 79–89 (2005).

[104] Fung, E. K., Planeta-Wilson, B., Mulnix, T. & Carson, R. E. A multimodal approach to image-derived input functions for brain PET. *IEEE Nucl Sci Symp Conf Rec* **2009**, 2710–2714 (2009).

[105] Mourik, J. E. *et al.* In vivo validation of reconstruction-based resolution recovery for human brain studies. *J Cereb Blood Flow Metab* **30**, 381–9 (2009).

[106] Croteau, E. *et al.* Image-derived input function in dynamic human PET/CT: methodology and validation with C-11-acetate and F-18-fluorothioheptadecanoic acid in muscle and F-18-fluorodeoxyglucose in brain. *Eur J Nucl Med Mol Imaging* **37**, 1539–1550 (2010).

[107] Hahn, A. *et al.* Combining image-derived and venous input functions enables quantification of serotonin-1A receptors with [carbonyl-11C]WAY-100635 independent of arterial sampling. *NeuroImage* **62**, 199–206 (2012).

[108] Chen, K. *et al.* Noninvasive quantification of the cerebral metabolic rate for glucose using positron emission tomography, 18F-fluoro-2-deoxyglucose, the Patlak method, and an image-derived input function. *J Cereb Blood Flow Metab* **18**, 716–23 (1998).

[109] Chen, K. *et al.* Characterization of the image-derived carotid artery input function using independent component analysis for the quantitation of [18F] fluorodeoxyglucose positron emission tomography images. *Phys Med Biol* **52**, 7055–71 (2007).

[110] Mourik, J. E. *et al.* Partial volume corrected image derived input functions for dynamic PET brain studies: methodology and validation for [11C]flumazenil. *NeuroImage* **39**, 1041–50 (2008).

[111] Liptrot, M. *et al.* Cluster analysis in kinetic modelling of the brain: a noninvasive alternative to arterial sampling. *NeuroImage* **21**, 483–93 (2004).

[112] MacQueen, J. Some methods for classification and analysis of multivariate observations. *Proc. Fifth Berkeley Symp. on Math. Statist. and Prob.* **1**, 281–297 (1967).

[113] Naganawa, M. *et al.* Extraction of a plasma time-activity curve from dynamic brain PET images based on independent component analysis. *IEEE Trans Biomed Eng* **52**, 201–10 (2005).

[114] Bodvarsson, B., Morkebjerg, M., Hansen, L. K., Knudsen, G. M. & Svarer, C. Extraction of time activity curves from positron emission tomography: K-means clustering or non-negative matrix factorization. *NeuroImage* **31**, T185–T186 (2006).

[115] Zanotti-Fregonara, P. *et al.* Comparison of eight methods for the estimation of the image-derived input function in dynamic [18F]-FDG PET human brain studies. *J Cereb Blood Flow Metab* **29**, 1825–35 (2009).

[116] Zanotti-Fregonara, P., Chen, K., Liow, J. S., Fujita, M. & Innis, R. B. Image-derived input function for brain PET studies: many challenges and few opportunities. *J Cereb Blood Flow Metab* **31**, 1986–98 (2011).

[117] Krejza, J. *et al.* Carotid artery diameter in men and women and the relation to body and neck size. *Stroke* **37**, 1103–5 (2006).

[118] Kerber, C. W. & Heilman, C. B. Flow dynamics in the human carotid artery: I. Preliminary observations using a transparent elastic model. *AJNR Am J Neuroradiol* **13**, 173–80 (1992).

[119] Johnson, A. E. *et al.* AZD2184: a radioligand for sensitive detection of beta-amyloid deposits. *J Neurochem* **108**, 1177–86 (2009).

[120] Jureus, A. *et al.* Characterization of AZD4694, a novel fluorinated Abeta plaque neuroimaging PET radioligand. *J Neurochem* **114**, 784–94 (2010).

[121] Cselenyi, Z. *et al.* Clinical validation of 18F-AZD4694, an amyloid-beta-specific PET radioligand. *J Nucl Med* **53**, 415–24 (2012).

[122] Forsberg, A. *et al.* Low background and high contrast PET imaging of amyloid-beta with [11C]AZD2995 and [11C]AZD2184 in Alzheimer's disease patients. *Eur J Nucl Med Mol Imaging* 580–93 (2013).

[123] Prince, M. *et al.* The global prevalence of dementia: a systematic review and meta-analysis. *Alzheimers Dement* **9**, 63–75 (2013).

[124] Wimo, A., Jonsson, L., Bond, J., Prince, M. & Winblad, B. The worldwide economic impact of dementia 2010. *Alzheimers Dement* **9**, 1–11 (2013).

[125] Mangialasche, F. and Solomon, A. and Winblad, B. and Mecocci, P. and Kivipelto, M. Alzheimer's disease: clinical trials and drug development. *Lancet Neurol* **9**, 702–16 (2010).

[126] Villemagne, V. L. *et al.* Amyloid beta deposition, neurodegeneration, and cognitive decline in sporadic Alzheimer's disease: a prospective cohort study. *Lancet Neurol* **12**, 357–67 (2013).

[127] Jack, J., C. R. *et al.* Hypothetical model of dynamic biomarkers of the Alzheimer's pathological cascade. *Lancet Neurol* **9**, 119–28 (2010).

[128] Jack, J., C. R. *et al.* An operational approach to National Institute on Aging-Alzheimer's Association criteria for preclinical Alzheimer disease. *Ann Neurol* **71**, 765–75 (2012).

[129] Jack, J., C. R. *et al.* Tracking pathophysiological processes in Alzheimer's disease: an updated hypothetical model of dynamic biomarkers. *Lancet Neurol* **12**, 207–16 (2013).

[130] Klunk, W. E. *et al.* Imaging brain amyloid in Alzheimer's disease with Pittsburgh Compound-B. *Ann Neurol* **55**, 306–19 (2004).

[131] Klunk, W. E. Amyloid imaging as a biomarker for cerebral beta-amyloidosis and risk prediction for Alzheimer dementia. *Neurobiol Aging* **32**, S20–S36 (2011).

[132] Yang, L., Rieves, D. & Ganley, C. Brain amyloid imaging–FDA approval of florbetapir F18 injection. *N Engl J Med* **367**, 885–7 (2012).

[133] Aizenstein, H. J. *et al.* Frequent Amyloid Deposition Without Significant Cognitive Impairment Among the Elderly. *Arch Neurol* **65**, 1509–1517 (2008).

[134] Mintun, M. A. *et al.* [11C]PIB in a nondemented population: potential antecedent marker of Alzheimer disease. *Neurology* **67**, 446–52 (2006).

[135] Rowe, C. C. *et al.* Amyloid imaging results from the australian imaging, biomarkers and lifestyle (aibl) study of aging. *Neurobiol Aging* **31**, 1275–83 (2010).

[136] Ong, K. *et al.* [18F]-florbetaben Abeta imaging in mild cognitive impairment. *Alzheimers Res Ther* **5**, 4 (2013).

[137] Villemagne, V. L. *et al.* Amyloid imaging with [18]F-florbetaben in Alzheimer disease and other dementias. *J Nucl Med* **52**, 1210–7 (2011).

[138] Barthel, H. *et al.* Cerebral amyloid-beta PET with florbetaben (F-18) in patients with Alzheimer's disease and healthy controls: a multicentre phase 2 diagnostic study. *Lancet Neurol* **10**, 424–435 (2011).

[139] Mormino, E. C. *et al.* Not quite pib-positive, not quite pib-negative: slight pib elevations in elderly normal control subjects are biologically relevant. *Neuroimage* **59**, 1152–60 (2012).

[140] Ng, S. *et al.* Visual assessment versus quantitative assessment of 11C-PIB PET and 18F-FDG PET for detection of Alzheimer's disease. *J Nucl Med* **48**, 547–52 (2007).

[141] Forsberg, A. *et al.* PET imaging of amyloid deposition in patients with mild cognitive impairment. *Neurobiol Aging* **29**, 1456–1465 (2008).

[142] van Velden, F. H. *et al.* HRRT versus HR+ human brain PET studies: an interscanner test-retest study. *J Nucl Med* **50**, 693–702 (2009).

[143] Pierson, M. E. *et al.* [11C]AZ10419369: a selective 5-HT1B receptor radioligand suitable for positron emission tomography (PET). Characterization in the primate brain. *NeuroImage* **41**, 1075–85 (2008).

[144] Varnas, K., Hall, H., Bonaventure, P. & Sedvall, G. Autoradiographic mapping of 5-HT(1B) and 5-HT(1D) receptors in the post mortem human brain using [3H]GR 125743. *Brain Res* **915**, 47–57 (2001).

[145] Varnas, K., Halldin, C. & Hall, H. Autoradiographic distribution of serotonin transporters and receptor subtypes in human brain. *Hum Brain Mapp* **22**, 246–260 (2004).

[146] Mengod, G., Cortés, R., Vilaró, M. & Hoyer, D. Distribution of 5-HT Receptors in the Cnetral Nervous System. In Müller, C. & Jacobs, B. (eds.) *Handbook of Behavioral Neurobiology of Serotonin*, vol. 1, 123–138 (Elsevier Academic Press, London, 2010), 1 edn.

[147] Andersson, J. D. *et al.* Radiosynthesis of the candidate beta-amyloid radioligand [11C]AZD2184: Positron emission tomography examination and metabolite analysis in cynomolgus monkeys. *Synapse* **64**, 733–41 (2010).

[148] Delforge, J. *et al.* Quantification of Benzodiazepine Receptors in Human Brain Using PET, [C-11] Flumazenil, and a Single-Experiment Protocol. *J Cerebr Blood Flow Metab* **15**, 284–300 (1995).

[149] Nyberg, S. *et al.* Detection of amyloid in Alzheimer's disease with positron emission tomography using [11C]AZD2184. *Eur J Nucl Med Mol Imaging* **36**, 1859–63 (2009).

[150] Varnas, K. *et al.* Quantitative analysis of [11C]AZ10419369 binding to 5-HT1B receptors in human brain. *J Cereb Blood Flow Metab* **31**, 113–23 (2011).

[151] Varrone, A. *et al.* Positron emission tomography imaging of 5-hydroxytryptamine receptors in parkinson's disease. *Neurobiol Aging* (2013). In press.

[152] Bergstrom, M. *et al.* Head fixation device for reproducible position alignment in transmission ct and positron emission tomography. *J Comput Assist Tomogr* **5**, 136–41 (1981).

[153] Roland, P. *et al.* Human brain atlas: For high-resolution functional and anatomical mapping. *Hum Brain Mapp* **1**, 173–184 (1993).

[154] Benjaminsson, S., Fransson, P. & Lansner, A. A novel model-free data analysis technique based on clustering in a mutual information space: application to resting-state fMRI. *Front Syst Neurosci* **4**, 1–8 (2010).

[155] Sperling, R. A. *et al.* Amyloid deposition is associated with impaired default network function in older persons without dementia. *Neuron* **63**, 178–188 (2009).

[156] Vannini, P. *et al.* Age and amyloid-related alterations in default network habituation to stimulus repetition. *Neurobiol Aging* **33**, 1237–52 (2012).

[157] Tuominen, L., Nummenmaa, L., Keltikangas-Jarvinen, L., Raitakari, O. & Hietala, J. Mapping neurotransmitter networks with PET: An example on serotonin and opioid systems. *Hum Brain Mapp* (2013).

[158] Geworski, L., Knoop, B. O., de Cabrejas, M. L., Knapp, W. H. & Munz, D. L. Recovery correction for quantitation in emission tomography: a feasibility study. *Eur J Nucl Med* **27**, 161–9 (2000).

[159] Mikhno, A., Zanderigo, F., Naganawa, M., Laine, A. F. & Parsey, R. V. Brain tissue selection procedures for image derived input functions derived using independent components analysis. *Conf Proc IEEE Eng Med Biol Soc* **2012**, 5987–90 (2012).

[160] Pichler, B. J., Judenhofer, M. S. & Pfannenberg, C. Multimodal imaging approaches: PET/CT and PET/MRI. *Handb Exp Pharmacol* 109–32 (2008).

[161] Pichler, B. J., Kolb, A., Nagele, T. & Schlemmer, H. P. PET/MRI: paving the way for the next generation of clinical multimodality imaging applications. *J Nucl Med* **51**, 333–6 (2010).

[162] Judenhofer, M. S. & Cherry, S. R. Applications for preclinical PET/MRI. *Semin Nucl Med* **43**, 19–29 (2013).

[163] Savli, M. *et al.* Normative database of the serotonergic system in healthy subjects using multi-tracer PET. *NeuroImage* **63**, 447–59 (2012).

[164] Zanotti-Fregonara, P. *et al.* Population-based input function and image-derived input function for [11C](R)-rolipram PET imaging: methodology, validation and application to the study of major depressive disorder. *NeuroImage* **63**, 1532–41 (2012).

[165] Ogden, R. T., Zanderigo, F., Choy, S., Mann, J. J. & Parsey, R. V. Simultaneous estimation of input functions: an empirical study. *J Cereb Blood Flow Metab* **30**, 816–26 (2010).

[166] Syvanen, S. *et al.* Predicting brain concentrations of drug using positron emission tomography and venous input: modeling of arterial-venous concentration differences. *Eur J Clin Pharmacol* **62**, 839–48 (2006).

[167] Pitsiu, M., Gries, J. M., Benowitz, N., Gourlay, S. G. & Verotta, D. Modeling nicotine arterial-venous differences to predict arterial concentrations and input based on venous measurements: application to smokeless tobacco and nicotine gum. *J Pharmacokinet Pharmacodyn* **29**, 383–402 (2002).

[168] Dubois, B. *et al.* Research criteria for the diagnosis of Alzheimer's disease: revising the NINCDS-ADRDA criteria. *Lancet Neurol* **6**, 734–46 (2007).